Measurements of B → J/ψ at forward rapidity in p + p collisions at √s=510 GeV

(PHENIX Collaboration) Adare, A.; ...; Dumancic, Mirta; ...; Makek, Mihael; ...; Zou, L.

Measurements of $B \to J/\psi$ at forward rapidity in $p+p$ collisions at $\sqrt{s} = 510$ GeV

C. Aidala,[39,43] N. N. Ajitanand,[61,†] Y. Akiba,[56,57,*] R. Akimoto,[12] J. Alexander,[61] M. Alfred,[23] K. Aoki,[32,56] N. Apadula,[28,62] H. Asano,[35,56] E. T. Atomssa,[62] A. Attila,[17] T. C. Awes,[52] C. Ayuso,[43] B. Azmoun,[7] V. Babintsev,[24] M. Bai,[6] X. Bai,[11] B. Bannier,[62] K. N. Barish,[8] S. Bathe,[5,57] V. Baublis,[55] C. Baumann,[7] S. Baumgart,[56] A. Bazilevsky,[7] M. Beaumier,[8] R. Belmont,[13,67] A. Berdnikov,[59] Y. Berdnikov,[59] D. Black,[8] D. S. Blau,[34] M. Boer,[39] J. S. Bok,[50] K. Boyle,[57] M. L. Brooks,[39] J. Bryslawskyj,[5,8] H. Buesching,[7] V. Bumazhnov,[24] C. Butler,[20] S. Butsyk,[49] S. Campbell,[14,28] C. CanoaRoman,[62] C.-H. Chen,[57] C. Y. Chi,[14] M. Chiu,[7] I. J. Choi,[25] J. B. Choi,[10,†] S. Choi,[60] P. Christiansen,[40] T. Chujo,[66] V. Cianciolo,[52] B. A. Cole,[14] M. Connors,[20,57] N. Cronin,[44,62] N. Crossette,[44] M. Csanád,[17] T. Csörgő,[31,69] T. W. Danley,[51] A. Datta,[49] M. S. Daugherity,[1] G. David,[7] K. DeBlasio,[49] K. Dehmelt,[62] A. Denisov,[24] A. Deshpande,[57,62] E. J. Desmond,[7] L. Ding,[28] J. H. Do,[70] L. D'Orazio,[41] O. Drapier,[36] A. Drees,[62] K. A. Drees,[6] M. Dumancic,[68] J. M. Durham,[39] A. Durum,[24] T. Elder,[20,31] T. Engelmore,[14] A. Enokizono,[56,58] S. Esumi,[66] K. O. Eyser,[7] B. Fadem,[44] W. Fan,[62] N. Feege,[62] D. E. Fields,[49] M. Finger,[9] M. Finger, Jr.,[9] F. Fleuret,[36] S. L. Fokin,[34] J. E. Frantz,[51] A. Franz,[7] A. D. Frawley,[19] Y. Fukao,[32] Y. Fukuda,[66] T. Fusayasu,[46] K. Gainey,[1] C. Gal,[62] P. Garg,[3,62] A. Garishvili,[64] I. Garishvili,[38] H. Ge,[62] F. Giordano,[25] A. Glenn,[38] X. Gong,[61] M. Gonin,[36] Y. Goto,[56,57] R. Granier de Cassagnac,[36] N. Grau,[2] S. V. Greene,[67] M. Grosse Perdekamp,[25] Y. Gu,[61] T. Gunji,[12] H. Guragain,[20] T. Hachiya,[57] J. S. Haggerty,[7] K. I. Hahn,[18] H. Hamagaki,[12] S. Y. Han,[18] J. Hanks,[62] S. Hasegawa,[29] T. O. S. Haseler,[20] K. Hashimoto,[56,58] R. Hayano,[12] X. He,[20] T. K. Hemmick,[62] T. Hester,[8] J. C. Hill,[28] K. Hill,[13] R. S. Hollis,[8] K. Homma,[22] B. Hong,[33] T. Hoshino,[22] N. Hotvedt,[28] J. Huang,[7,39] S. Huang,[67] T. Ichihara,[56,57] Y. Ikeda,[56] K. Imai,[29] Y. Imazu,[56] M. Inaba,[66] A. Iordanova,[8] D. Isenhower,[1] A. Isinhue,[44] Y. Ito,[47] D. Ivanishchev,[55] B. V. Jacak,[62] S. J. Jeon,[45] M. Jezghani,[20] Z. Ji,[62] J. Jia,[7,61] X. Jiang,[39] B. M. Johnson,[7,20] K. S. Joo,[45] V. Jorjadze,[62] D. Jouan,[53] D. S. Jumper,[25] J. Kamin,[62] S. Kanda,[12,32] B. H. Kang,[21] J. H. Kang,[70] J. S. Kang,[21] D. Kapukchyan,[8] J. Kapustinsky,[39] S. Karthas,[62] D. Kawall,[42] A. V. Kazantsev,[34] J. A. Key,[49] V. Khachatryan,[62] P. K. Khandai,[3] A. Khanzadeev,[55] K. M. Kijima,[22] C. Kim,[8,33] D. J. Kim,[30] E.-J. Kim,[10] M. Kim,[60] M. H. Kim,[33] Y.-J. Kim,[25] Y. K. Kim,[21] D. Kincses,[17] E. Kistenev,[7] J. Klatsky,[19] D. Kleinjan,[8] P. Kline,[62] T. Koblesky,[13] M. Kofarago,[17,69] B. Komkov,[55] J. Koster,[57] D. Kotchetkov,[51] D. Kotov,[55,59] F. Krizek,[30] S. Kudo,[66] K. Kurita,[58] M. Kurosawa,[56,57] Y. Kwon,[70] R. Lacey,[61] Y. S. Lai,[14] J. G. Lajoie,[28] E. O. Lallow,[44] A. Lebedev,[28] D. M. Lee,[39] G. H. Lee,[10] J. Lee,[18,63] K. B. Lee,[39] K. S. Lee,[33] S. H. Lee,[62] M. J. Leitch,[39] M. Leitgab,[25] Y. H. Leung,[62] B. Lewis,[62] N. A. Lewis,[43] X. Li,[11] X. Li,[39] S. H. Lim,[39,70] L. D. Liu,[54] M. X. Liu,[39] V.-R. Loggins,[25] S. Lokos,[17] D. Lynch,[7] C. F. Maguire,[67] Y. I. Makdisi,[6] M. Makek,[68,71] A. Manion,[62] V. I. Manko,[34] E. Mannel,[7] M. McCumber,[13,39] P. L. McGaughey,[39] D. McGlinchey,[13,19] C. McKinney,[25] A. Meles,[50] M. Mendoza,[8] B. Meredith,[25] Y. Miake,[66] T. Mibe,[32] A. C. Mignerey,[41] D. E. M. Mihalik,[62] A. Milov,[68] D. K. Mishra,[4] J. T. Mitchell,[7] G. Mitsuka,[57] S. Miyasaka,[56,65] S. Mizuno,[56,66] A. K. Mohanty,[4] S. Mohapatra,[61] T. Moon,[70] D. P. Morrison,[7] S. I. M. Morrow,[67] M. Moskowitz,[44] T. V. Moukhanova,[34] T. Murakami,[35,56] J. Murata,[56,58] A. Mwai,[61] T. Nagae,[35] K. Nagai,[65] S. Nagamiya,[32,56] K. Nagashima,[22] T. Nagashima,[58] J. L. Nagle,[13] M. I. Nagy,[17] I. Nakagawa,[56,57] H. Nakagomi,[56,66] Y. Nakamiya,[22] K. R. Nakamura,[35,56] T. Nakamura,[56] K. Nakano,[56,65] C. Nattrass,[64] P. K. Netrakanti,[4] M. Nihashi,[22,56] T. Niida,[66] R. Nouicer,[7,57] T. Novák,[31,69] N. Novitzky,[30,62] R. Novotny,[15] A. S. Nyanin,[34] E. O'Brien,[7] C. A. Ogilvie,[28] H. Oide,[12] K. Okada,[57] J. D. Orjuela Koop,[13] J. D. Osborn,[43] A. Oskarsson,[40] K. Ozawa,[32] R. Pak,[7] V. Pantuev,[26] V. Papavassiliou,[50] I. H. Park,[18,63] J. S. Park,[60] S. Park,[56,60,62] S. K. Park,[33] S. F. Pate,[50] L. Patel,[20] M. Patel,[28] J.-C. Peng,[25] W. Peng,[67] D. V. Perepelitsa,[7,13,14] G. D. N. Perera,[50] D. Yu. Peressounko,[34] C. E. PerezLara,[62] J. Perry,[28] R. Petti,[7,62] M. Phipps,[7,25] C. Pinkenburg,[7] R. P. Pisani,[7] A. Pun,[51] M. L. Purschke,[7] H. Qu,[1] P. V. Radzevich,[59] J. Rak,[30] I. Ravinovich,[68] K. F. Read,[52,64] D. Reynolds,[61] V. Riabov,[48,55] Y. Riabov,[55,59] E. Richardson,[41] D. Richford,[5] T. Rinn,[28] N. Riveli,[51] D. Roach,[67] S. D. Rolnick,[8] M. Rosati,[28] Z. Rowan,[5] J. Runchey,[28] M. S. Ryu,[21] B. Sahlmueller,[62] N. Saito,[32] T. Sakaguchi,[7] H. Sako,[29] V. Samsonov,[48,55] M. Sarsour,[20] K. Sato,[66] S. Sato,[29] S. Sawada,[32] B. Schaefer,[67] B. K. Schmoll,[64] K. Sedgwick,[8] J. Seele,[57] R. Seidl,[56,57] Y. Sekiguchi,[12] A. Sen,[20,28,64] R. Seto,[8] P. Sett,[4] A. Sexton,[41] D. Sharma,[62] A. Shaver,[28] I. Shein,[24] T.-A. Shibata,[56,65] K. Shigaki,[22] M. Shimomura,[28,47] K. Shoji,[56] P. Shukla,[4] A. Sickles,[7,25] C. L. Silva,[39] D. Silvermyr,[40,52] B. K. Singh,[3] C. P. Singh,[3] V. Singh,[3] M. J. Skoby,[43] M. Skolnik,[44] M. Slunečka,[9] K. L. Smith,[19] S. Solano,[44] R. A. Soltz,[38] W. E. Sondheim,[39] S. P. Sorensen,[64] I. V. Sourikova,[7] P. W. Stankus,[52] P. Steinberg,[7] E. Stenlund,[40] M. Stepanov,[42,†] A. Ster,[69] S. P. Stoll,[7] M. R. Stone,[13] T. Sugitate,[22] A. Sukhanov,[7] J. Sun,[62] S. Syed,[20] A. Takahara,[12] A. Taketani,[56,57] Y. Tanaka,[46] K. Tanida,[29,57,60] M. J. Tannenbaum,[7] S. Tarafdar,[3,67,68] A. Taranenko,[48,61] G. Tarnai,[16] E. Tennant,[50] R. Tieulent,[20] A. Timilsina,[28] T. Todoroki,[56,66] M. Tomášek,[15,27] H. Torii,[12] C. L. Towell,[1] R. S. Towell,[1] I. Tserruya,[68] Y. Ueda,[22] B. Ujvari,[16] H. W. van Hecke,[39] M. Vargyas,[17,69] S. Vazquez-Carson,[13] E. Vazquez-Zambrano,[14] A. Veicht,[14] J. Velkovska,[67] R. Vértesi,[69] M. Virius,[15] V. Vrba,[15,27] E. Vznuzdaev,[55] X. R. Wang,[50,57] Z. Wang,[5] D. Watanabe,[22] K. Watanabe,[56,58] Y. Watanabe,[56,57] Y. S. Watanabe,[12,32] F. Wei,[50] S. Whitaker,[28] S. Wolin,[25] C. P. Wong,[20] C. L. Woody,[7] M. Wysocki,[52] B. Xia,[51] C. Xu,[50] Q. Xu,[67]

Y. L. Yamaguchi,[12,57,62] A. Yanovich,[24] P. Yin,[13] S. Yokkaichi,[56,57] J. H. Yoo,[33] I. Yoon,[60] Z. You,[39] I. Younus,[37,49] H. Yu,[50,54] I. E. Yushmanov,[34] W. A. Zajc,[14] A. Zelenski,[6] S. Zharko,[59] S. Zhou,[11] and L. Zou[8]

(PHENIX Collaboration)

[1]*Abilene Christian University, Abilene, Texas 79699, USA*
[2]*Department of Physics, Augustana University, Sioux Falls, South Dakota 57197, USA*
[3]*Department of Physics, Banaras Hindu University, Varanasi 221005, India*
[4]*Bhabha Atomic Research Centre, Bombay 400 085, India*
[5]*Baruch College, City University of New York, New York, New York, 10010 USA*
[6]*Collider-Accelerator Department, Brookhaven National Laboratory, Upton, New York 11973-5000, USA*
[7]*Physics Department, Brookhaven National Laboratory, Upton, New York 11973-5000, USA*
[8]*University of California-Riverside, Riverside, California 92521, USA*
[9]*Charles University, Ovocný trh 5, Praha 1, 116 36, Prague, Czech Republic*
[10]*Chonbuk National University, Jeonju 561-756, Korea*
[11]*Science and Technology on Nuclear Data Laboratory, China Institute of Atomic Energy, Beijing 102413, People's Republic of China*
[12]*Center for Nuclear Study, Graduate School of Science, University of Tokyo, 7-3-1 Hongo, Bunkyo, Tokyo 113-0033, Japan*
[13]*University of Colorado, Boulder, Colorado 80309, USA*
[14]*Columbia University, New York, New York 10027 and Nevis Laboratories, Irvington, New York 10533, USA*
[15]*Czech Technical University, Zikova 4, 166 36 Prague 6, Czech Republic*
[16]*Debrecen University, H-4010 Debrecen, Egyetem tér 1, Hungary*
[17]*ELTE, Eötvös Loránd University, H-1117 Budapest, Pázmány P. s. 1/A, Hungary*
[18]*Ewha Womans University, Seoul 120-750, Korea*
[19]*Florida State University, Tallahassee, Florida 32306, USA*
[20]*Georgia State University, Atlanta, Georgia 30303, USA*
[21]*Hanyang University, Seoul 133-792, Korea*
[22]*Hiroshima University, Kagamiyama, Higashi-Hiroshima 739-8526, Japan*
[23]*Department of Physics and Astronomy, Howard University, Washington, D.C. 20059, USA*
[24]*IHEP Protvino, State Research Center of Russian Federation, Institute for High Energy Physics, Protvino 142281, Russia*
[25]*University of Illinois at Urbana-Champaign, Urbana, Illinois 61801, USA*
[26]*Institute for Nuclear Research of the Russian Academy of Sciences, prospekt 60-letiya Oktyabrya 7a, Moscow 117312, Russia*
[27]*Institute of Physics, Academy of Sciences of the Czech Republic, Na Slovance 2, 182 21 Prague 8, Czech Republic*
[28]*Iowa State University, Ames, Iowa 50011, USA*
[29]*Advanced Science Research Center, Japan Atomic Energy Agency, 2-4 Shirakata Shirane, Tokai-mura, Naka-gun, Ibaraki-ken 319-1195, Japan*
[30]*Helsinki Institute of Physics and University of Jyväskylä, P.O. Box 35, FI-40014 Jyväskylä, Finland*
[31]*Károly Róberts University College, H-3200 Gyöngyös, Mátrai út 36, Hungary*
[32]*KEK, High Energy Accelerator Research Organization, Tsukuba, Ibaraki 305-0801, Japan*
[33]*Korea University, Seoul 136-701, Korea*
[34]*National Research Center "Kurchatov Institute," Moscow 123098 Russia*
[35]*Kyoto University, Kyoto 606-8502, Japan*
[36]*Laboratoire Leprince-Ringuet, Ecole Polytechnique, CNRS-IN2P3, Route de Saclay, F-91128 Palaiseau, France*
[37]*Physics Department, Lahore University of Management Sciences, Lahore 54792, Pakistan*
[38]*Lawrence Livermore National Laboratory, Livermore, California 94550, USA*
[39]*Los Alamos National Laboratory, Los Alamos, New Mexico 87545, USA*
[40]*Department of Physics, Lund University, Box 118, SE-221 00 Lund, Sweden*
[41]*University of Maryland, College Park, Maryland 20742, USA*
[42]*Department of Physics, University of Massachusetts, Amherst, Massachusetts 01003-9337, USA*
[43]*Department of Physics, University of Michigan, Ann Arbor, Michigan 48109-1040, USA*
[44]*Muhlenberg College, Allentown, Pennsylvania 18104-5586, USA*
[45]*Myongji University, Yongin, Kyonggido 449-728, Korea*
[46]*Nagasaki Institute of Applied Science, Nagasaki-shi, Nagasaki 851-0193, Japan*
[47]*Nara Women's University, Kita-uoya Nishi-machi Nara 630-8506, Japan*

[48]National Research Nuclear University, MEPhI, Moscow Engineering Physics Institute, Moscow 115409, Russia
[49]University of New Mexico, Albuquerque, New Mexico 87131, USA
[50]New Mexico State University, Las Cruces, New Mexico 88003, USA
[51]Department of Physics and Astronomy, Ohio University, Athens, Ohio 45701, USA
[52]Oak Ridge National Laboratory, Oak Ridge, Tennessee 37831, USA
[53]IPN-Orsay, Univ. Paris-Sud, CNRS/IN2P3, Université Paris-Saclay, BP1, F-91406 Orsay, France
[54]Peking University, Beijing 100871, People's Republic of China
[55]PNPI, Petersburg Nuclear Physics Institute, Gatchina, Leningrad region 188300, Russia
[56]RIKEN Nishina Center for Accelerator-Based Science, Wako, Saitama 351-0198, Japan
[57]RIKEN BNL Research Center, Brookhaven National Laboratory, Upton, New York 11973-5000, USA
[58]Physics Department, Rikkyo University, 3-34-1 Nishi-Ikebukuro, Toshima, Tokyo 171-8501, Japan
[59]Saint Petersburg State Polytechnic University, St. Petersburg, 195251 Russia
[60]Department of Physics and Astronomy, Seoul National University, Seoul 151-742, Korea
[61]Chemistry Department, Stony Brook University, SUNY, Stony Brook, New York 11794-3400, USA
[62]Department of Physics and Astronomy, Stony Brook University, SUNY, Stony Brook, New York 11794-3800, USA
[63]Sungkyunkwan University, Suwon 440-746, Korea
[64]University of Tennessee, Knoxville, Tennessee 37996, USA
[65]Department of Physics, Tokyo Institute of Technology, Oh-okayama, Meguro, Tokyo 152-8551, Japan
[66]Center for Integrated Research in Fundamental Science and Engineering, University of Tsukuba, Tsukuba, Ibaraki 305, Japan
[67]Vanderbilt University, Nashville, Tennessee 37235, USA
[68]Weizmann Institute, Rehovot 76100, Israel
[69]Institute for Particle and Nuclear Physics, Wigner Research Centre for Physics, Hungarian Academy of Sciences (Wigner RCP, RMKI) H-1525 Budapest 114, P.O. Box 49, Budapest, Hungary
[70]Yonsei University, IPAP, Seoul 120-749, Korea
[71]Department of Physics, Faculty of Science, University of Zagreb, Bijenička 32, HR-10002 Zagreb, Croatia

(Received 6 January 2017; published 2 May 2017)

We report the first measurement of the fraction of J/ψ mesons coming from B-meson decay ($F_{B\to J/\psi}$) in $p+p$ collisions at $\sqrt{s}=510$ GeV. The measurement is performed using the forward silicon vertex detector and central vertex detector at PHENIX, which provide precise tracking and distance-of-closest-approach determinations, enabling the statistical separation of J/ψ due to B-meson decays from prompt J/ψ. The measured value of $F_{B\to J/\psi}$ is $8.1\% \pm 2.3\%(\text{stat}) \pm 1.9\%(\text{syst})$ for J/ψ with transverse momenta $0 < p_T < 5$ GeV/c and rapidity $1.2 < |y| < 2.2$. The measured fraction $F_{B\to J/\psi}$ at PHENIX is compared to values measured by other experiments at higher center of mass energies and to fixed-order-next-to-leading-logarithm and color-evaporation-model predictions. The $b\bar{b}$ cross section per unit rapidity $[d\sigma/dy(pp \to b\bar{b})]$ extracted from the obtained $F_{B\to J/\psi}$ and the PHENIX inclusive J/ψ cross section measured at 200 GeV scaled with color-evaporation-model calculations, at the mean B hadron rapidity $y=\pm 1.7$ in 510 GeV $p+p$ collisions, is $3.63^{+1.92}_{-1.70}$ μb. It is consistent with the fixed-order-next-to-leading-logarithm calculations.

DOI: 10.1103/PhysRevD.95.092002

I. INTRODUCTION

The measurement of bottom (B) mesons in $p+p$ and $p+\bar{p}$ collisions is of interest to constrain the total bottom cross section as well as test our understanding of bottom quark production mechanisms and hadronization. There are extensive direct measurements of various B mesons, as well as measurements of $B \to J/\psi$ contributions over a broad range in J/ψ transverse momentum and rapidity from the Tevatron in $p+\bar{p}$ at $\sqrt{s}=1.8$, 1.96 TeV [1–3] and the Large Hadron Collider (LHC) in $p+p$ at $\sqrt{s}=7$–13 TeV [4–8]. In contrast, measurements from UA1 in $p+\bar{p}$ at $\sqrt{s}=630$ GeV [9] are statistically limited and only for $p_T(J/\psi) > 5$ GeV/c. Adding new measurements at lower energies and covering different kinematic regions is valuable for testing perturbative quantum chromodynamics

*PHENIX Spokesperson.
akiba@rcf.rhic.bnl.gov
†Deceased.

(pQCD) calculations and constraining production mechanisms.

The Relativistic Heavy Ion Collider (RHIC) provides $p+p$ collisions at $\sqrt{s}=200$, 500 and 510 GeV, which extends the kinematic reach for bottom measurements. At these smaller energies, bottom production is dominated by gluon-gluon fusion, while higher energy bottom production contains a larger fraction of flavor excitation and gluon splitting processes [10]. The STAR experiment measured $B\to J/\psi$ at midrapidity for J/ψ $p_T>5$ GeV/c in $p+p$ at $\sqrt{s}=200$ GeV [11]. Our measurement at forward rapidity and p_T within 0–5 GeV/c in $\sqrt{s}=510$ GeV $p+p$ collisions at PHENIX can provide the validation of parton distribution functions (PDFs) in a different gluon fractional momentum range $5\times10^{-4}<x_{Bj}<1\times10^{-2}$. As the highest center of mass energy accessed by RHIC collisions, bottom measurements at $\sqrt{s}=510$ GeV will also help us understand the energy dependence from RHIC to LHC energies.

Inclusive J/ψ production has a component referred to as "prompt," which includes direct J/ψ production, as well as decays from ψ' and χ_c. The term prompt is in contrast to "nonprompt," which specifically refers to production through more long-lived decay parent hadrons (i.e. B mesons). The nonprompt J/ψ component that comes from the decay of B mesons provides a clean channel to measure B-meson yields. At forward rapidities, the time dilation of the B lifetime leads to a larger displacement from the event vertex before decaying to J/ψ. We use this displacement to separate J/ψ originating from B-meson decay from prompt J/ψ through measurement of the decay particle's distance of closest approach (DCA) to the primary event vertex.

In this paper, the ratio of J/ψ from B-meson decays to inclusive J/ψ ($F_{B\to J/\psi}$) is determined for J/ψ kinematics in the range of $0<p_T<5$ GeV/c and rapidity $1.2<|y|<2.2$ through DCA distributions in $p+p$ collisions at $\sqrt{s}=510$ GeV, using the PHENIX muon arms plus the forward and central silicon vertex tracker detectors. The $b\bar{b}$ cross section per unit rapidity at the mean B hadron rapidity $y=\pm1.7$ in 510 GeV $p+p$ collisions is extracted from the obtained $F_{B\to J/\psi}$ and the PHENIX inclusive J/ψ cross section measured at 200 GeV, scaled with color-evaporation-model (CEM) calculations [12].

The paper is organized as follows. Section II discusses the PHENIX detector setup for this analysis, in particular the central and forward silicon vertex detectors which are used for the primary vertex and the DCA determination. Section III describes the data reconstruction and simulation setup, signal and background determination, and fitting procedure. The acceptance × efficiency correction factor to achieve final results and the systematic uncertainty evaluation are discussed in Sec. III as well. The results and interpretation are discussed in Sec. IV and the conclusions are summarized in Sec. V.

II. EXPERIMENTAL SETUP

The data set used in this analysis is from the 2012 run of $p+p$ at $\sqrt{s}=510$ GeV and the detector configuration of PHENIX for that running period is shown in Fig. 1. For this measurement, the beam-beam counters (BBC) [13], the muon arm spectrometers [14], the central silicon vertex detector (VTX) [15,16] and the forward silicon vertex detector (FVTX) [17] are used. The BBC detector, which comprises 128 quartz Čerenkov counters with a pseudorapidity coverage of $3.0<|\eta|<3.9$, determines when a collision event has taken place. The BBC provides the minimum-bias (MB) trigger, by requiring a coincidence between at least one hit in both the positive- and negative-rapidity acceptance of the BBC.

The PHENIX muon detectors are divided into the north ($1.2<y<2.4$) and the south ($-2.2<y<-1.2$) arms. Each muon arm spectrometer has full azimuthal coverage and is composed of hadron absorbers, a muon tracker (MuTr) which resides in a radial field magnet, and a muon identifier (MuID). The MuTr comprises three cathode strip wire chamber stations inside a magnet which provides a radial magnetic field with an integrated bending power of around 0.8 T · m. The MuTr measures track momentum p with a resolution of $\delta p/p\approx0.05$ at $p<10$ GeV/c. The hadron absorber comprises 19 cm of copper, 60 cm of iron and 36.2 cm of stainless steel along the beam axis. The absorbers are situated in front of the MuTr to provide hadron (mostly pion and kaon) rejection. The MuTr has a position resolution at each station of around 100 μm, which, together with a precisely determined vertex, results in a mass resolution of around 95 MeV for dimuon pairs within the J/ψ mass region and $0<p_T(J/\psi)<5$ GeV/c. The downstream MuID comprises five sandwiched planes of Iarocci proportional tubes and steel. The MuTr + MuID system together with the steel absorbers have approximately 10 interaction lengths of material. In this analysis, the dimuon trigger is used which requires two muonlike trajectories (defined as a "road") passing through at least three MuID planes with at least one reaching the last plane of the MuID.

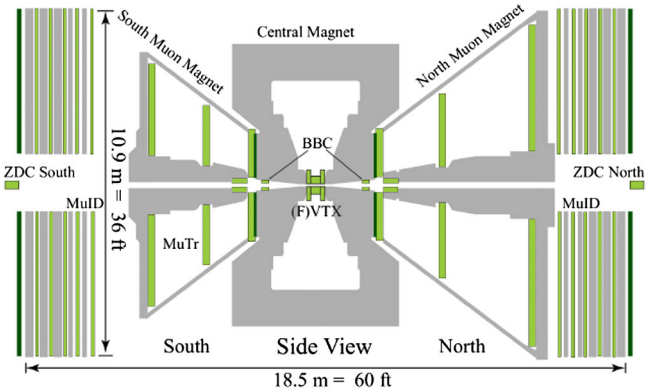

FIG. 1. The PHENIX detector setup for the 510 GeV $p+p$ data taking in 2012.

The VTX (installed in 2011) comprises two inner pixel layers and two outer strip layers distributed from 2.5 to 14.0 cm along the radial direction, covering $\Delta\varphi \approx 5.0$ radians in azimuth and $|z(\mathrm{VTX})| < 10$ cm along the z axis (beam direction). The radii of the inner silicon pixel detectors are 2.5 and 5.0 cm, and the radii of the outer silicon strip detectors are on average 10.0 and 14.0 cm. Each pixel of the inner VTX layers covers a 50 μm × 450 μm active area [15,16]. The FVTX, installed in front of the hadron absorbers in 2012, comprises eight silicon disks perpendicular to the beam axis and placed at approximately $z = \pm 20.1$, ± 26.1, ± 32.2 and ± 38.2 cm. The rapidity coverage of the FVTX overlaps the muon arm coverage. Each FVTX disk comprises 48 individual silicon sensors (wedges) and each wedge contains two columns of strips that each span an azimuthal segmentation of 3.75°. The column comprises mini strips with 75 μm width in the radial direction. The strip length in the azimuthal (φ) direction varies from 3.4 mm at the inner radius to 11.5 mm at the outer radius for the largest stations [17]. Tracks passing through the forward muon arms are unlikely to pass through the VTX outer strip layers due to the angular acceptance of the strips. In addition, the two inner pixel layers can help improve the DCA resolutions as they are closer to the vertex and have finer pixel sizes compared to the outer strip layers. Therefore, for track reconstruction with the combined FVTX + VTX detectors, only the two inner pixel layers in the VTX are used.

The FVTX enhances the existing muon arm tracking performance in several ways. The FVTX helps reject hadrons that undergo multiple scattering or decay inside the hadron absorber by requiring a good joint fit of FVTX and MuTr tracks. It also provides a better opening angle determination than the MuTr alone can provide, which results in an improved mass resolution for dimuon pairs. Finally, the additional precision tracking added in front of the hadron absorber by the FVTX makes the measurement of displaced tracks possible when combined with a determination of the primary vertex position.

Due to limited resolutions in the z and azimuthal φ components of the FVTX detector, the separation of prompt and decay muons is realized with the FVTX using the DCA measurement instead of measuring the displaced vertex of decayed muons. Because the FVTX has better resolution in the radial direction than in the azimuthal direction, the radial DCA ($\mathrm{DCA_R}$) is the primary variable used in this analysis. The primary vertex is reconstructed using all FVTX and VTX tracks which pass the track quality cut $\chi^2/\mathrm{NDF} < 4$, where NDF is the number of degrees of freedom. Figure 2 illustrates the projection of a muon from a B meson to J/ψ decay in the transverse vertex plane and how to calculate the $\mathrm{DCA_R}$. A track reconstructed in the FVTX is extrapolated to the transverse plane (x-y) at the z location of the primary collision vertex. DCA is defined as the vector $\vec{L}_{\mathrm{DCA}}$ formed between this intersection point and the x-y collision vertex point in the same transverse plane of the collision vertex. The $\mathrm{DCA_R}$ is the component of the DCA which is measured in the same radial direction as the FVTX strips,

$$\mathrm{DCA_R} \equiv \vec{L}_{\mathrm{DCA}} \cdot \hat{R} = \vec{L}_{\mathrm{DCA}} \cdot \frac{\vec{R}}{|\vec{R}|}. \quad (1)$$

Prompt particles from the primary collision vertex have a symmetric $\mathrm{DCA_R}$ distribution centered at zero, with the width determined by the intrinsic detector and vertex resolutions, while the shape is asymmetric for decay particles from a displaced decay vertex. As illustrated in Fig. 2(b), the definition of $\mathrm{DCA_R}$ results in an asymmetric distribution for muons from $B \to J/\psi$ decay due to the projection onto the transverse x-y plane of the primary vertex. This is confirmed by the full simulation shown in Sec. III C.

III. ANALYSIS PROCEDURE

This analysis starts with the identification of good J/ψ candidates by selecting dimuon pairs found by the MuTr that are matched to MuID tracks. Separately, track finding is performed in the FVTX/VTX system where reconstructed tracks are required to contain at least one FVTX hit and a total of at least three FVTX + VTX hits. Then, for each

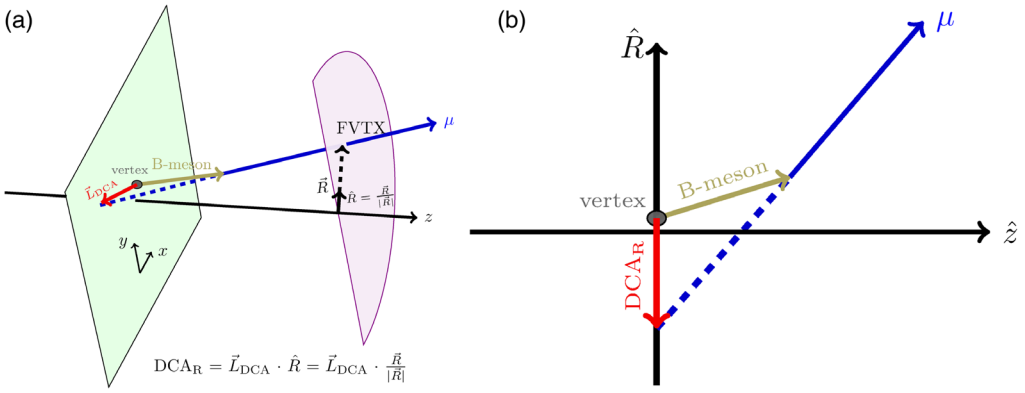

FIG. 2. (a) 3D and (b) 2D projection of a muon from a B meson to J/ψ to dimuon decay to the transverse vertex plane (x-y) and definition of $\mathrm{DCA_R}$.

reconstructed MuTr track, the FVTX/VTX tracks are searched for potential matches.

The collision point is determined from VTX and FVTX tracks. First, regions where there is a concentration of track crossings are determined. The center of gravity of each of these regions defines a collision point. For each region, the center of gravity is used to initiate a minimization of the vector sum of the DCAs of the tracks. During the minimization, tracks with large displacements are removed to improve the fidelity of the final vertex reconstruction. The vertex determination in each event is strongly affected by the small VTX and FVTX track multiplicities in $p+p$ collisions. Events containing $b\bar{b}$ decay products can also skew the vertex determination. Therefore, in this analysis we take advantage of the beam stability in x and y during the fill (5–12 hours) and use the measured average x and y position of all events in the fill to determine our primary x and y vertex. The spread of the primary x and y vertex position based on the beam spot size is around 80 μm in RMS. The z position is still determined on an event-by-event basis for events that have a VTX + FVTX track multiplicity ≥ 2. Events with smaller multiplicity are thrown out. For events with more than one reconstructed vertex, the vertex with the best reconstruction quality is selected as the primary vertex. For the reconstructed events, we obtain an average z resolution of approximately 180 μm in 510 GeV $p+p$ collisions. After matching to the FVTX tracks, the $\mathrm{DCA_R}$ is determined using the MuTr + MuID + FVTX/VTX combined track fit and the primary vertex location.

The next step in the analysis is to characterize the $\mathrm{DCA_R}$ of muons from prompt J/ψ decay and J/ψ from B-meson decay through simulation. The final analysis step uses a fit function for the muon $\mathrm{DCA_R}$ spectra that includes the prompt J/ψ, J/ψ from B-meson decay, and background components to extract the fraction of J/ψ from B-meson decay in the data, using a log-likelihood fit. Details of the analysis procedure are explained step by step in the following sections.

A. Data quality assurance

The precise primary z-vertex reconstruction is limited by the VTX acceptance and therefore only events within a z-vertex (z_{VTX}) window of $(-10, 10)$ cm are selected for this analysis. Events with poorly determined primary z vertices are removed by requiring less than 400 μm calculated uncertainty on the z vertex. Runs without an accurately determined average x, y position of the beam center are rejected. The number of events with MB and dimuon triggers surviving after these vertex selections is 3.5×10^9, which is equivalent to a total integrated luminosity of 0.47 pb^{-1}. The event rejection fraction is around 67%.

During the 2012 $p+p$ run, there were some areas of the FVTX detector which were not yet operational due to various electronics issues. When the FVTX-MuTr matching algorithm tries to find an FVTX track in a dead area, there is a tendency for it to match to a track in a live region neighboring the dead one instead, pulling the matching distributions away from the central value of 0. Because of this tendency to pull tracks away from a symmetric distribution, fiducial cuts are applied to remove tracks that point to the vicinity of a dead region in the FVTX detector.

Detector misalignments can shift the projected track position in the vertex plane and thus distort the $\mathrm{DCA_R}$ distributions. Before proceeding with the data analysis, alignment corrections are applied to the data in two stages, before and after the track reconstruction. The preproduction alignment left residual φ-dependent misalignments, which were up to 100 μm in certain detector regions. Tilts which shift the FVTX silicon sensors out of the normal x-y plane were corrected in a postproduction alignment procedure, reducing the final misalignment values to less than 30 μm.

A final verification of the FVTX alignment to the VTX, which is the most critical alignment for DCA analyses, is performed using real data. Tracks which show MuID activity in the fourth Iarocci tube plane (gap), but not in the last gap are first selected. The majority of these tracks are from stopped hadrons, which are predominantly prompt particles, and provide a high statistics sample for studying alignment. Events with a large vertex uncertainty, tracks next to dead areas, and bad quality FVTX tracks are removed from this sample. To remove the hadron decay component, a minimum longitudinal momentum cut of ($p_z > 4$ GeV/c) is required. After the misalignment corrections described above are applied, the $\mathrm{DCA_R}$ is then extracted for these tracks and checked for any indications of residual misalignments. The mean of these distributions is found to be flat along the φ direction (within the measurement precision) and the overall offsets of the distributions are within 30 μm in both arms. These offset values are much smaller than the detector position resolution. Variations of the $\mathrm{DCA_R}$ mean and spread which could occur if there were beam instability, detector, trigger or acceptance × efficiency changes, are checked by examining the $\mathrm{DCA_R}$ distributions as a function of run and BBC instantaneous rate. The mean values of the $\mathrm{DCA_R}$ distributions across all runs are found to be within 1 standard deviation (of the intrinsic $\mathrm{DCA_R}$ distribution width) after quality assurance checks.

B. J/ψ reconstruction

Tracks formed in the MuTr are required to contain at least 12 (out of 16) hits in the various cathode strip planes. We start with a loose quality cut $\chi^2/\mathrm{NDF} < 10$ on the MuTr tracks to make sure all potentially good tracks are included in the analysis. The MuTr tracks which reach the last gap of the MuID and have longitudinal momentum >3 GeV/c are treated as muon track candidates. Muon candidates in this analysis need to have good associations between the MuTr track and the MuID road in both position and angle. The momentum-dependent position and angle differences

TABLE I. Quality cuts for J/ψ candidates in $p+p$ collisions.

Variable (Meaning)	$1.2 < \lvert y \rvert < 2.2$
$\lvert z_{\mathrm{VTX}} \rvert$ (collision vertex measured by the FVTX/VTX)	<10 cm
$\lvert z_{\mathrm{VTX}}$uncertainty$\rvert$ (collision vertex uncertainty measured by the FVTX/VTX)	<400 μm
$p \cdot DG0$ (Track momentum times the spatial difference between the MuTr and MuID tracks at the first MuID layer)	<80 GeV$/c \cdot$ cm
$p \cdot DDG0$ (Track momentum times the slope difference between the MuTr and MuID tracks at the first MuID layer)	<40 GeV$/c \cdot {}^\circ$
χ^2_{MuTr} (χ^2/NDF of the MuTr track)	<10
χ^2_{MuID} (χ^2/NDF of the MuID road)	<3
Track $\chi^2_{\mathrm{FVTX-MuTr}}$ (χ^2/NDF of the FVTX-MuTr matching μ track)	<5
Radial residual between FVTX and MuTr projections at FVTX station 4	$<3\sigma$
Azimuthal residual between FVTX and MuTr projections at FVTX station 4	$<3\sigma$
Last gap (Last MuID plane that the μ track penetrated)	$=4$
Nidhits (Number of hits in the MuID, out of the maximum 10)	>6
Ntrhits (Number of hits in the MuTr, out of the maximum 16)	>11
Nfvtxhits (Number of hits in the FVTX + VTX, out of the maximum 6)	>2
$\lvert p_z \rvert$(GeV$/c$) (Momentum of the μ along the beam axis)	>3
Dimuon pair vertex χ^2/NDF	<3

between the MuTr track and the MuID road are required to be within 3 standard deviations as calculated using the Kalman Filter track fitting and error propagation method. In addition, the associated MuID road should contain at least 6 (out of 10) hits in different MuID planes. Because the MuID road is not included in the fully reconstructed tracks, we apply a tighter quality cut which is $\chi^2/\mathrm{NDF} < 3$.

Good matching between the FVTX tracks and the MuTr + MuID tracks is also required. This requirement helps remove misreconstructed and bad quality tracks as well as some hadronic background. The matched FVTX tracks should contain at least 3 (out of 6 potential) FVTX + VTX hits. The differences in azimuthal angle, polar angle and radial distance between matched FVTX and MuTr + MuID combined tracks are required to be within 3 standard deviations as determined by the Kalman Filter fits and error propagation. Fits on the combined FVTX + MuTr tracks should satisfy $\chi^2/\mathrm{NDF} < 5$. Dimuon pairs are created from muons passing all the quality cuts. A slightly different selection which requires at least one muon of the dimuon pair passing through the quality cuts is tested. No bias is found as consistent results are achieved between the two selections. The fit of the vertex point plus the two muon tracks with opposite charges must satisfy $\chi^2/\mathrm{NDF} < 3$ to ensure the two muon tracks are not separated by more than 1 mm at the vertex point. The complete set of quality cuts is listed in Table I.

Raw yields of the invariant mass of dimuon pairs after applying the quality cuts are shown in Figs. 3(a) and 3(b). A smaller number of events is measured in the forward than the backward rapidity due to larger MuTr dead areas and lower MuID efficiency in the forward rapidity region during this data taking period. These spectra contain a combination of J/ψ events, combinatorial background (random combinations of reconstructed tracks within an event) and heavy flavor background. The heavy flavor background determination will be discussed in Sec. III E 3. Two methods are used to extract the combinatorial background. One uses the like-sign dimuon pairs within events, and the other uses the unlike-sign dimuon pairs in mixed events. To match the yields of the analyzed mixed events to the (same) events, a normalization scale $\mathrm{Norm}_{\mathrm{mix}}$, defined in Eq. (2), is applied to the mass distribution of dimuon pairs and muon $\mathrm{DCA_R}$ distribution in mixed events:

$$\mathrm{Norm}_{\mathrm{mix}} = \sqrt{\frac{N^{\mathrm{same}}_{++} \cdot N^{\mathrm{same}}_{--}}{N^{\mathrm{mix}}_{++} \cdot N^{\mathrm{mix}}_{--}}} \tag{2}$$

where N^{same}_{++}, N^{same}_{--} are the like-sign yields in same events and N^{mix}_{++}, N^{mix}_{--} are the like-sign yields in mixed events, for dimuon mass ≥ 2 GeV$/c^2$. As shown in Fig. 3, the invariant mass distributions determined by these methods are consistent with each other within statistical uncertainties. The mixed event method is then used to determine the combinatorial background for the final analysis in order to reduce statistical fluctuations. After the combinatorial background subtraction, clear J/ψ peaks are found in both muon arms, as shown in Figs. 3(c) and 3(d). A mass window cut ($2.7 < \mathrm{mass} < 3.5$ GeV$/c^2$) is applied to the dimuon pair invariant mass distribution to select J/ψ candidates. The signal (combinatorial background subtracted yields) to the combinatorial background ratio in the J/ψ mass window is 18.6 in the $1.2 < y < 2.2$ region and 19.9 in the $-2.2 < y < -1.2$ region.

C. Simulation setup

The full simulation framework, which comprises PYTHIA8[18]+GEANT4[19]+reconstruction, is set up to characterize the $\mathrm{DCA_R}$ distributions of muons from prompt J/ψ

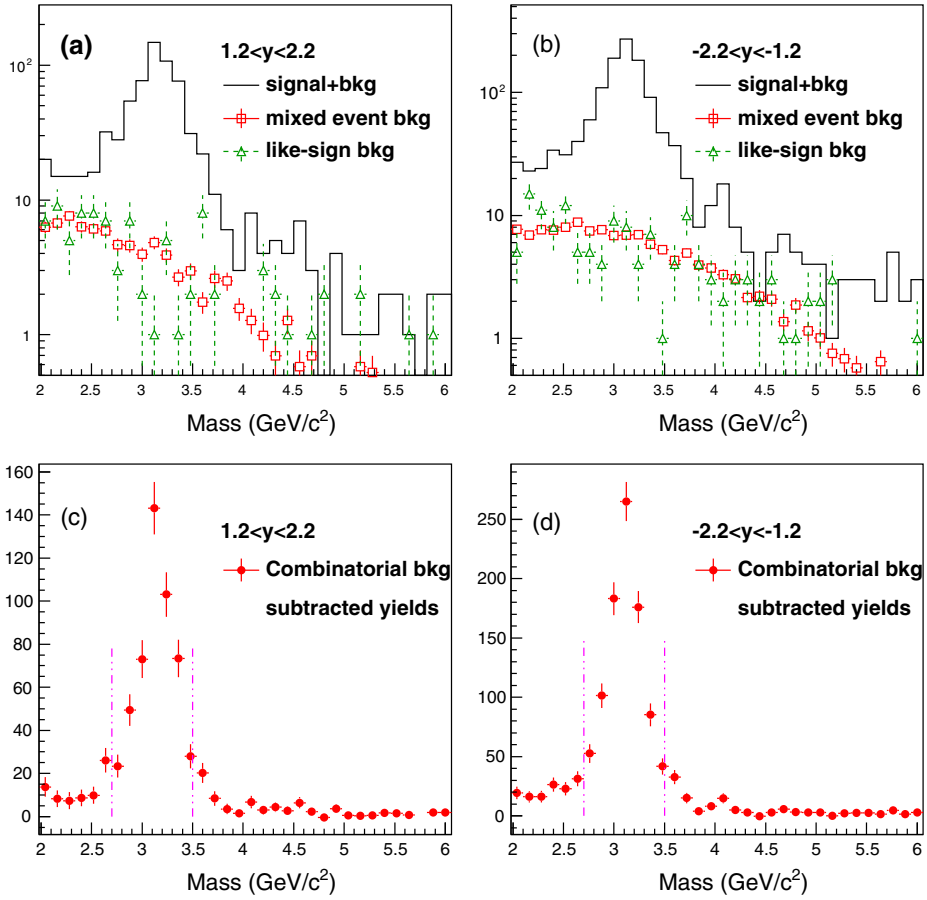

FIG. 3. The invariant mass of dimuons in the (a),(c) $1.2 < y < 2.2$ and (b),(d) $-2.2 < y < -1.2$ regions. Raw yields (black solid), the combinatorial background using mixed events (red open rectangular) and like-sign dimuon pairs (green open triangle) are shown in panels (a) and (b). The combinatorial background subtracted yields are shown in panels (c) and (d). The magenta dashed lines represent the mass cut used to select J/ψ candidates.

and J/ψ from B-meson decay. Dead areas in the detector are determined from data on a run-by-run basis and the same vertex and tracking reconstruction algorithms as in data analysis are used. The width of the simulated primary vertex distributions along the x and y axes is 80 μm as determined from Vernier Scan measurements [20]. The vertex distribution along the z axis used in the simulation has been determined from the real data. To get an accurately reproduced z-vertex resolution in simulation, which is dependent on the multiplicity in the event, additional simulated MB events (with z vertex matched to the hard QCD events) are embedded into the prompt J/ψ events, or events with a J/ψ from B-meson decay. To ensure that the accessed kinematic region of the probed PDF in the MB events is the same in prompt J/ψ events or in B-meson $\rightarrow$ J/ψ events, the renormalization scale Q^2_{renorm} defined in PYTHIA, which determines the PDF shape, is kept at the same value between the MB event and the triggered event.

To verify that the simulations accurately represent the real data, we have compared the simulated and measured muon $\mathrm{DCA_R}$ distributions from inclusive J/ψ events. The inclusive J/ψ events in simulation are obtained by combining 90% prompt J/ψ events and 10% J/ψ from B-meson decay. This fraction of B-meson decays to J/ψ is selected based on the average result from global data measured in the same inclusive J/ψ p_T region [3–7]. A single Gaussian function is fit to the centroid of the $\mathrm{DCA_R}$ distributions in data and simulation to derive the resolutions of the prompt component of the $\mathrm{DCA_R}$. The momentum dependence of this $\mathrm{DCA_R}$ resolution extracted from the core region ($|\mathrm{DCA_R}| < 500$ μm) is compared between data and simulation. As shown in Fig. 4, good agreement between data and simulation is achieved in both of the measured rapidity regions.

D. Signal determination

The shapes of the $\mathrm{DCA_R}$ distributions of muons from prompt J/ψ and those from B-meson $\rightarrow$ J/ψ are characterized using the full simulation. Figure 5 shows the resulting normalized distribution of $\mathrm{DCA_R}$ for muons from prompt J/ψ events (blue open circle) and from B-meson $\rightarrow$ J/ψ events (green circle). As explained at the end of Sec. II, the shape of the muon $\mathrm{DCA_R}$ distribution in prompt J/ψ

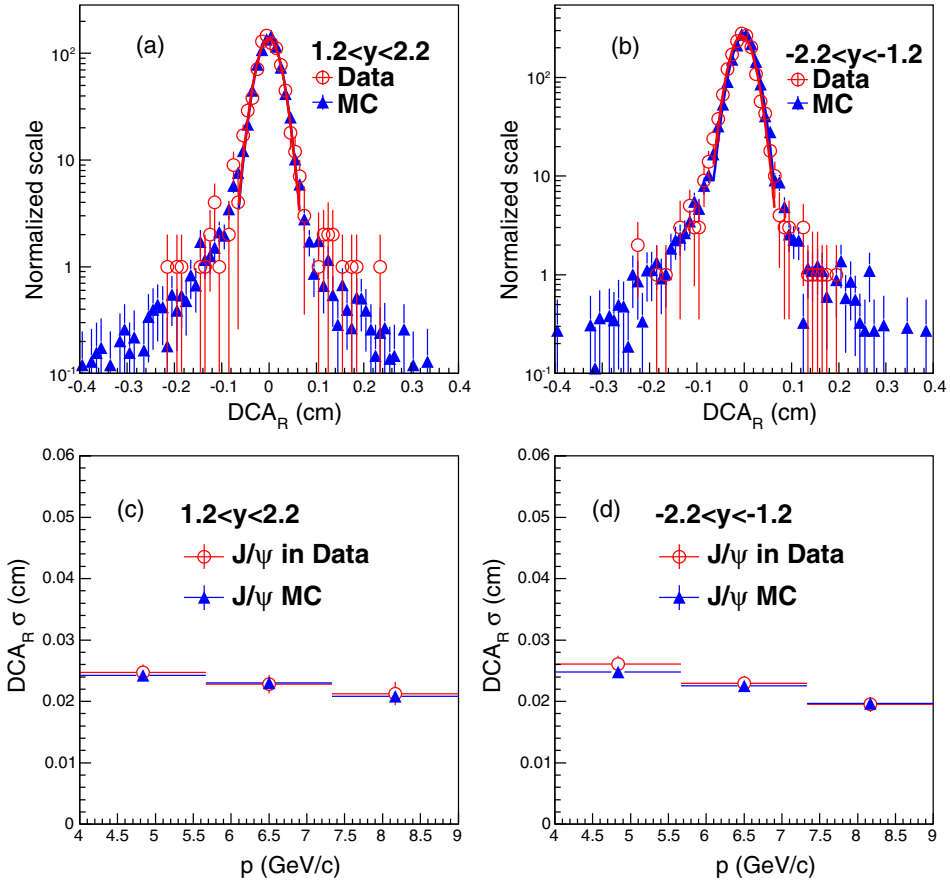

FIG. 4. Comparison of the normalized $\mathrm{DCA_R}$ distributions of single muons from inclusive J/ψ events in data (red open circle) and simulation (blue solid triangle). Panels (a) and (b) show the comparison for integrated momenta and panels (c) and (d) show the comparison for the momentum-dependent $\mathrm{DCA_R}$ resolution. There is good agreement between data and simulation.

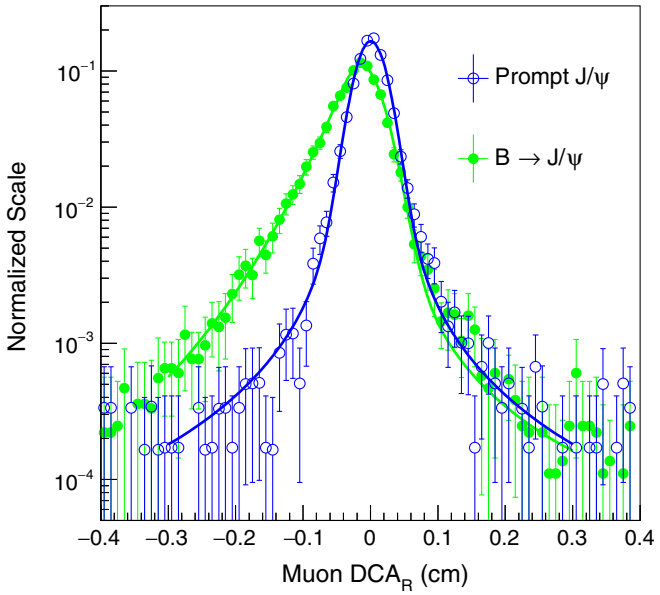

FIG. 5. Normalized $\mathrm{DCA_R}$ distributions of simulated prompt J/ψ (blue open circle) and B-meson $\to J/\psi$ events (green circle). The muon $\mathrm{DCA_R}$ distributions are normalized by the total number of entries in the $\mathrm{DCA_R}$ range of $(-0.4$ cm, 0.4 cm). Solid lines stand for the fits defined in Eq. (3) and Eq. (4).

events is symmetric, which is consistent with expectations for prompt particle decays. The Λ_b, $B^{\pm}$, B^0, B_s^0 hadrons have a finite lifetime of 1.4–1.6 ps on average, resulting in a displaced vertex at forward rapidity of approximately 0.8 mm from the primary collision vertex for the J/ψ from B-meson decay. Due to the displacement between the decay vertex and the primary collision vertex, the negative side of the muon $\mathrm{DCA_R}$ distribution shows a clear deviation from symmetry for B-meson $\to J/\psi$ events. The respectively symmetric and asymmetric $\mathrm{DCA_R}$ distributions allow the separation of prompt J/ψ from B-meson $\to J/\psi$.

Several functions were tested to describe the line shapes of the muon $\mathrm{DCA_R}$ in both prompt J/ψ and J/ψ from B-meson decay in simulations. The final fit functions which will be described below are selected based on the best fits to the simulation spectra with the maximum log-likelihood method and a convolution of the intrinsic $\mathrm{DCA_R}$ resolution with a function which represents B-meson decay kinematics is used. Variations of the fit functions and the simulation setup were then used to account for systematic uncertainties in the fit function. A convolution fit is used to describe the shape of the muon $\mathrm{DCA_R}$ from prompt J/ψ decay, with the definition shown in Eq. (3).

$$f_{\text{prompt}J/\psi}(\text{DCA}_\text{R}) = \frac{1}{\sqrt{2\pi}\sigma}\exp\left[-\frac{(\text{DCA}_\text{R}-\mu)^2}{2\sigma^2}\right] \otimes \frac{\sigma_1^2\text{DCA}_\text{R}^2}{(\text{DCA}_\text{R}^2-\mu_1^2)^2+\text{DCA}_\text{R}^4(\sigma_1^2/\mu_1^2)}, \quad (3)$$

where μ, σ, μ_1 and σ_1 are determined from the fit to the prompt J/ψ simulation spectra. Parameter σ and σ_1 determine the width of the muon DCA_R shape in prompt J/ψ events, which comes from the detector and vertex resolutions. Values of these parameters defined in Eq. (3) are fixed in the next step: the fit to the measured DCA_R distributions. For B-meson decay to J/ψ events, the convolution fit function defined in Eq. (4) is used:

$$f_{B\to J/\psi}(\text{DCA}_\text{R}) = f_{\text{prompt}J/\psi}(\text{DCA}_\text{R}) \otimes f_B(\text{DCA}_\text{R}), \quad (4)$$

where the function $f_{\text{prompt }J/\psi}(\text{DCA}_\text{R})$ is defined in Eq. (3). The parameters of $f_{\text{prompt }J/\psi}(\text{DCA}_\text{R})$ are already determined, as explained above, in the fit of muon DCA_R in the prompt J/ψ simulation. Function $f_B(\text{DCA}_\text{R})$, which stands for the decay kinematics of B meson, is defined as

$$f_B(\text{DCA}_\text{R}) = \begin{cases} \exp\left[-\frac{(\text{DCA}_\text{R}-\mu_2)^2}{2\sigma_2^2}\right], & \frac{\text{DCA}_\text{R}-\mu_2}{\sigma_2} > -\alpha \\ (\frac{n}{|\alpha|})^n \exp(-\frac{|\alpha|^2}{2})(\frac{n}{|\alpha|} - |\alpha| - \frac{\text{DCA}_\text{R}-\mu_2}{\sigma_2})^{-n}, & \frac{\text{DCA}_\text{R}-\mu_2}{\sigma_2} \le -\alpha \end{cases} \quad (5)$$

where μ_2, σ_2, n and α are parameters determined from the fit to the $B \to J/\psi \to \mu^+\mu^-$ simulation. The average value of the muon DCA_R from $B \to J/\psi$ decay is determined by μ_2. Parameters σ_2, n and α determine the asymmetric shape of this DCA_R distribution. The determined values of these parameters defined in this section and used in Eq. (4) and Eq. (5) are then fixed in the fit to the measured DCA_R distributions.

Fits of the simulated muon DCA_R distributions for prompt J/ψ (blue open circle) and B to J/ψ (green circle) are shown in Fig. 5. The DCA_R spectra can be modeled by the two functions defined in Eq. (3) and Eq. (4).

E. Background determination

For this analysis, backgrounds come from three different sources: combinatorial, MuTr-FVTX track mismatching and heavy flavor decay continuum which represents unlike-sign dimuon pairs from $b\bar{b} \to B\bar{B} \to \mu^+\mu^- + X$ and $c\bar{c} \to D\bar{D} \to \mu^+\mu^- + X$ events. The combinatorial background and the background from mismatching between FVTX and MuTr tracks are determined by data-driven methods. The fraction of the contribution from the heavy-flavor-continuum background is determined by fitting the dimuon pair invariant mass spectra in real data, and the DCA_R shape is determined from simulation. Details of the background determinations will be discussed in Secs. III E 1 through III E 3.

1. Combinatorial background determination

The combinatorial background, which comes from combining randomly associated tracks in an event, is evaluated using unlike-sign dimuons formed by muon tracks from two different events (referred to as the mixed event procedure). The events to be mixed are required to have z vertices with no more than 1.5 cm difference from each other. The muon DCA_R distribution of the combinatorial background from normalized mixed events [the normalization factor is defined in Eq. (2)] is shown as magenta open triangles in Fig. 6.

2. FVTX-MuTr mismatching determination

The last FVTX plane and the first MuTr station are 150 cm apart and have approximately 1 m of absorber material in between. MuTr tracks with momentum above 3 GeV/c projected to the fourth station of the FVTX therefore cover a circle with a radius of up to 2 cm for muons, due to the multiple scattering in the absorber. As a result, some fraction of the MuTr projections will find more than one FVTX track or a single but incorrect FVTX track inside its projected circle, and have a certain probability of selecting an incorrect FVTX match. We refer to these incorrect matches as "mismatching background."

To estimate the amount of mismatching, we attempt to match MuTr tracks from one event to FVTX tracks from a separate event (referred to as swapped events). To be as realistic as possible, the swapped events need to belong to the same z-vertex category, meaning the difference of the z vertex between the swapped event and the true event should be less than 1 mm. The selection of 1 mm z-vertex difference does not introduce any bias to the DCA_R distribution. In addition to this, we also count the mismatching tracks from swapped events only when the matching track in the swapped event has a better χ^2 than the matching track in the real event, so that we do not overestimate the mismatches in real events. The mismatching background in the analyzed events is dominated by J/ψ MuTr tracks which do not have a corresponding FVTX track in the real event and accidentally match to a random background track. The fraction of candidate FVTX tracks in swapped events which are found to be wrongly

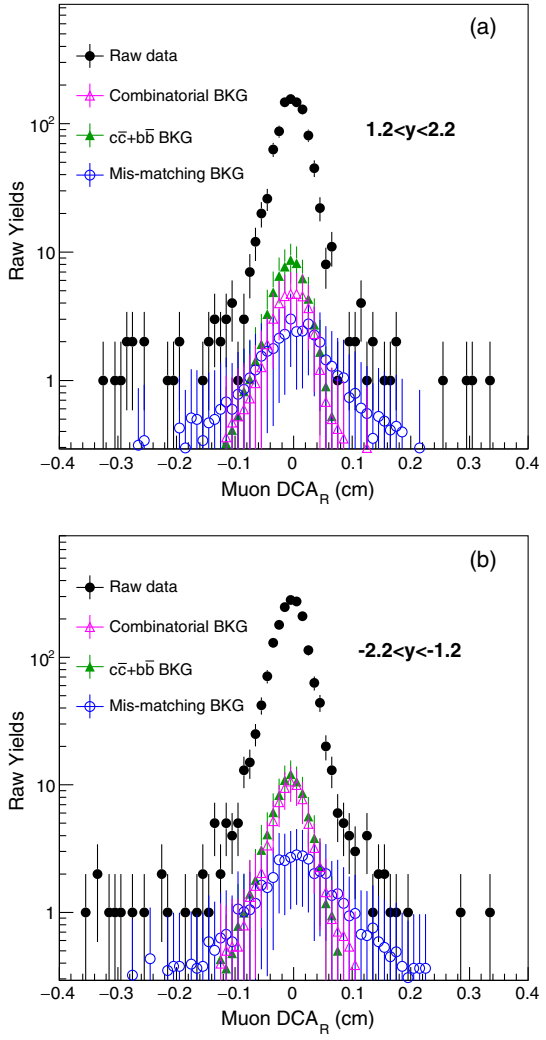

FIG. 6. The raw yields of data ([black] closed circles) and estimated background $\mathrm{DCA_R}$ distributions within the J/ψ mass window (2.7–3.5 GeV/c^2) are shown for (a) rapidity $1.2 < y < 2.2$ and (b) $-2.2 < y < -1.2$ The combinatorial background defined as $f_{\mathrm{combinatorial}}$ in Eq. (8) ([magenta] open triangle), the heavy-flavor-continuum ($c\bar{c} + b\bar{b}$) background defined as $f_{c\bar{c}+b\bar{b}}$ in Eq. (8) ([green] solid triangle) and the detector mismatching background defined as f_{mismatch} in Eq. (8) ([blue] open circle) are determined using techniques described in the text.

associated with a MuTr track from a good J/ψ dimuon pair, and that pass the quality cuts shown in Table I, is 3% (2%) in the $1.2 < y < 2.2$ ($-2.2 < y < -1.2$) rapidity region.

3. Heavy favor background determination

After subtracting the combinatorial background from the dimuon invariant mass distribution within the 2–6 GeV/c^2 region (shown in Fig. 3), there are remaining backgrounds in the sideband regions outside the J/ψ mass window. This remaining background is dominated by the heavy flavor continuum and indicates that this continuum is not negligible in the J/ψ mass region. To determine the fraction of the heavy flavor background, a fit function which includes yields from J/ψ, ψ', the combinatorial background and heavy-flavor-continuum background is applied to the invariant mass distribution of dimuon pairs. In the dimuon pair mass region >4 GeV/c^2, the heavy-flavor-continuum background also contains Drell-Yan. Because the fraction of Drell-Yan events within the J/ψ mass region (2.7–3.5 GeV/c^2) is negligible, the fit in this mass region does not include a Drell-Yan component.

Figure 7 shows the fit of the dimuon mass distribution to determine the heavy-flavor-continuum background. The total background (yellow) determined by the fit to the invariant mass spectrum, which comprises the combinatorial (red) and the heavy flavor background (blue), follows the mass distribution outside the J/ψ mass window well. The fraction of the heavy flavor background within the J/ψ mass window is found to be $7.1\% \pm 1.1\%$ ($5.5\% \pm 0.8\%$) in the $1.2 < y < 2.2$ ($-2.2 < y < -1.2$) regions.

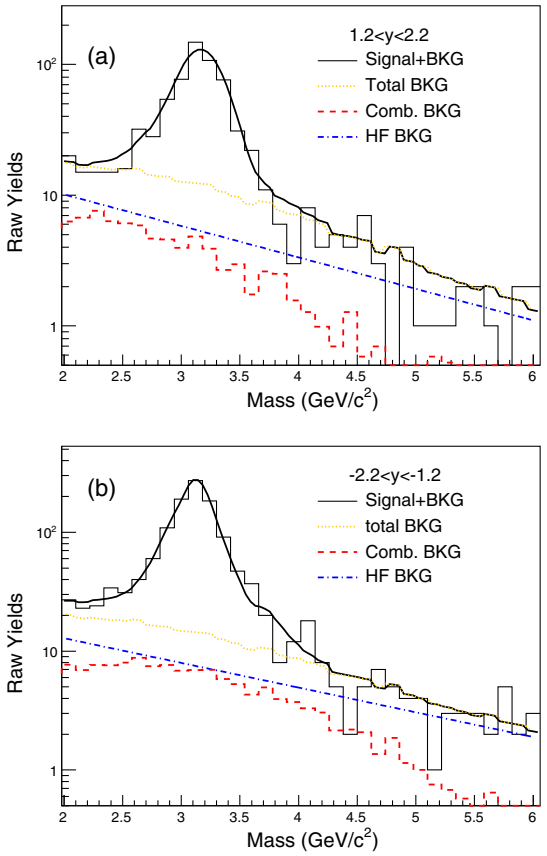

FIG. 7. Fit of dimuon mass spectra to determine the heavy-flavor-continuum background for (a) rapidity $1.2 < y < 2.2$ and (b) $-2.2 < y < -1.2$. The fit function ([black] solid curve) includes the J/ψ and $\psi\prime$ yields which already include the FVTX-MuTr mismatching background, the combinatorial background ([red] dashed curve) and the heavy-flavor-continuum background ([blue] dash-dotted curve). The total background ([yellow] solid-dotted curve) shows the combinatorial and the heavy-flavor-continuum background.

The relative $b\bar{b}$ and $c\bar{c}$ dimuon contributions within the J/ψ mass window are not well known, and extrapolation from previous midrapidity dimuon invariant mass yields in 200 GeV $p+p$ collisions would introduce a large systematic uncertainty. We therefore first fit the unlike-sign dimuon invariant mass spectrum near the J/ψ region including the PYTHIA8-simulated shape of $b\bar{b}$ and $c\bar{c}$ components and an unconstrained normalization scale to estimate the contribution. The fit suggests there is a 33% $b\bar{b}$ fraction in the heavy flavor continuum within the J/ψ mass region. However, we do note there is systematic uncertainty in the PYTHIA8 shape. Because of this uncertainty, for this analysis the fraction of the $b\bar{b}$ contribution to the heavy flavor yields within the J/ψ mass window is set to be 50%, and varied from 0 to 100% to take into account all possibilities in the systematic uncertainty.

F. Fitting procedure

The $\mathrm{DCA_R}$ distributions are selected from dimuon pairs within the mass window 2.7–3.5 GeV/c^2. A fit function is developed to simultaneously extract the prompt J/ψ and B-meson $\rightarrow J/\psi$ yields from the real data $\mathrm{DCA_R}$ distributions with the maximum log-likelihood method. This fit function comprises five components: (1) muons from prompt J/ψ, (2) muons from B-meson $\rightarrow J/\psi$, (3) combinatorial background determined by mixed events, (4) mismatching between FVTX and MuTr determined by swapped events, and (5) heavy flavor ($c\bar{c}+b\bar{b}$) continuum background. The fit function which is used to determine the shape of muon $\mathrm{DCA_R}$ distributions from prompt J/ψ (B-meson $\rightarrow J/\psi$) events is $f_{\mathrm{prompt}J/\psi}(\mathrm{DCA_R})$ [$f_{B\rightarrow J/\psi}(\mathrm{DCA_R})$] as discussed in Sec. III D. Parameters defined in both Eq. (3) and Eq. (4) are fixed according to the fit to the simulated spectra and the detector resolution smearing is fine-tuned in the data fit. The functions which represent the three background contributions are $f_{\mathrm{combinatorial}}(\mathrm{DCA_R})$, $f_{\mathrm{mismatch}}(\mathrm{DCA_R})$ and $f_{c\bar{c}+b\bar{b}}(\mathrm{DCA_R})$ as discussed in Sec. III E. Histograms of muon $\mathrm{DCA_R}$ from different background contributions after normalization are used to represent each component in Eq. (8). Fluctuations of the fit methods, signal and background determinations are studied in the systematic uncertainty evaluations. These functions used to describe the data spectrum are summarized in Eq. (6),

$$f_{\mathrm{total}}(\mathrm{DCA_R}) = f_{\mathrm{sig}}(\mathrm{DCA_R}) + f_{\mathrm{bkg}}(\mathrm{DCA_R}), \tag{6}$$

$$f_{\mathrm{sig}}(\mathrm{DCA_R}) = \mathrm{Yield}_{\mathrm{incl}\,J/\psi} \times [\mathrm{F}_{B\rightarrow J/\psi} \times f_{B\rightarrow J/\psi}(\mathrm{DCA_R}) + (1-\mathrm{F}_{B\rightarrow J/\psi}) \times f_{\mathrm{prompt}\,J/\psi}(\mathrm{DCA_R})], \tag{7}$$

$$f_{\mathrm{bkg}}(\mathrm{DCA_R}) = f_{\mathrm{combinatorial}}(\mathrm{DCA_R}) + f_{\mathrm{mismatch}}(\mathrm{DCA_R}) + f_{c\bar{c}+b\bar{b}}(\mathrm{DCA_R}), \tag{8}$$

where $\mathrm{Yield}_{\mathrm{incl}\,J/\psi}$ is the total yield of inclusive J/ψ which comprises both prompt J/ψ and B-meson decayed J/ψ. Normalization and shapes of most of the components are fixed in previous steps. In the final stage of the fit, the fraction of muons from B-meson $\rightarrow J/\psi$ (i.e. $F_{B\rightarrow J/\psi}$), is the main free parameter in the total fit function [defined in Eq. (6)], together with the J/ψ yield and a last tuning of the resolution that is described below. As the $\mathrm{DCA_R}$ resolution in data can be affected by additional factors which may not be well captured by the simulation (such as event-by-event variations in the vertex resolution, additional smearing from multiple scattering in the nonuniform detector materials, part of the detector randomly dropping out within a run and beam-beam collision geometry fluctuations), an additional free parameter, $\sigma\prime$, is introduced in the convolution fit functions for prompt J/ψ [defined in Eq. (3)] and B-meson $\rightarrow J/\psi$ [defined in Eq. (4)]. It accounts for detector resolution smearing and also captures any uncertainty of the beam spot size. The fit is then performed with the parameter σ_1^* instead of σ_1, where $\sigma_1^* = \sigma_1 + \sigma\prime$. The resolution smearing parameter $\sigma\prime$ determined from the fit to the data is within 20 μm with approximately 20 μm statistical uncertainty for the $1.2 < |y| < 2.2$ region. The size of the smearing is much smaller than the average x-y beam profile value (around 80 μm) and the $\mathrm{DCA_R}$ resolution (around 230 μm). The value of the resolution smearing $\sigma\prime$ varies from 5 to 70 μm when different beam profile values in the x-y plane are used in the simulation (from 80 to 180 μm). Variation of the smearing parameter $\sigma\prime$ will be included in the systematic uncertainty evaluation. Applying the fit procedure to the $\mathrm{DCA_R}$ distributions, assuming 50% of the heavy-flavor-continuum contribution comes from $b\bar{b}$ (see discussions in III E 3), allows the raw fraction of J/ψ mesons from B decays in inclusive J/ψ yields to be extracted. The corresponding raw ratios $B \rightarrow J/\psi$ are $7.3\% \pm 3.7\%(\mathrm{stat})$ for $(1.2 < y < 2.2)$ and $8.1\% \pm 2.8\%(\mathrm{stat})$ for $(-2.2 < y < -1.2)$. The spectra and fit results are shown in Fig. 8. The fit parameter values are summarized in Table II.

G. Acceptance × efficiency correction

In $p+p$ collisions, the $\mathrm{DCA_R}$ resolution is dominated by the VTX/FVTX vertex resolution. Higher event multiplicity can lead to a better vertex resolution and a higher probability that a vertex can be reconstructed for a given event. The $B \rightarrow J/\psi$ events have higher average VTX/FVTX multiplicity in comparison with prompt J/ψ events. Conversely, due to their different p_T distributions, $B \rightarrow J/\psi$ events have a somewhat lower probability of having both muons accepted into the muon arm than prompt J/ψ events. These differences in VTX/FVTX event multiplicities and kinematics result in somewhat different values of the acceptance × efficiency for the two sets of events. The raw ratio $F^{\mathrm{raw}}_{B\rightarrow J/\psi}$ as discussed in Sec. III F must be

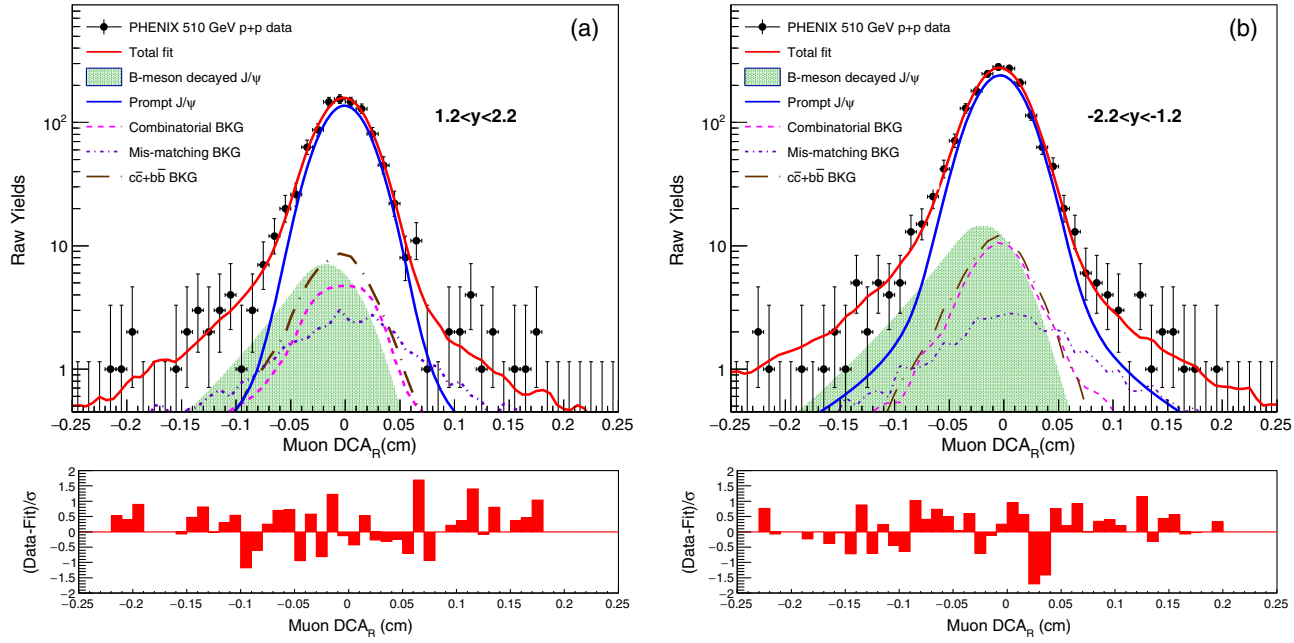

FIG. 8. $B \to J/\psi$ fraction fit to muon $\mathrm{DCA_R}$ in the (a) $1.2 < y < 2.2$ and (b) $-2.2 < y < -1.2$ regions. The ([red] solid curve) stands for the total fit, which includes the prompt J/ψ (solid blue), the B-meson $\to J/\psi$ ([green] filled region), the combinatorial background ([magenta] dashed curve), the $c\bar{c} + b\bar{b}$ background ([brown] long-dashed curve) and the detector mismatching background ([purple] short-dashed curve).

corrected for the relative acceptance × efficiency difference between prompt J/ψ and $B \to J/\psi$ events, using the PYTHIA8 + GEANT4 + reconstruction simulation described previously in Sec. III C, $\frac{A\varepsilon_{\mathrm{prompt}J/\psi\to\mu\mu}}{A\varepsilon_{B\to J/\psi\to\mu\mu}}$, where $A\varepsilon_{\mathrm{prompt}J/\psi\to\mu\mu}$ ($A\varepsilon_{B\to J/\psi\to\mu\mu}$) is the acceptance×efficiency for prompt J/ψ ($B \to J/\psi$) events.

The acceptance × efficiency for prompt J/ψ events is $0.455\% \pm 0.007\%$ ($0.506\% \pm 0.008\%$) and for $B \to J/\psi$ events is $0.446\% \pm 0.007\%$ ($0.473\% \pm 0.007\%$) in the $-2.2 < y < -1.2$ ($1.2 < y < 2.2$) rapidity region. The extracted relative ratio of $B \to J/\psi$ acceptance × efficiency to prompt J/ψ acceptance × efficiency is 0.980 ± 0.022 (0.935 ± 0.020) in the $-2.2 < y < -1.2$ ($1.2 < y < 2.2$) rapidity region. The $B \to J/\psi$ fraction $F_{B\to J/\psi}$ which is defined as $\frac{N_{B\to J/\psi}}{N_{\mathrm{prompt}J/\psi}+N_{B\to J/\psi}}$ ($N_{\mathrm{prompt}J/\psi}$ is the yield for prompt J/ψ, $N_{B\to J/\psi}$ is the yield for $B \to J/\psi$) can be derived according to Eq. (9).

$$F_{B\to J/\psi} = \frac{1}{1 + (\frac{1}{F^{\mathrm{raw}}_{B\to J/\psi}} - 1) \cdot \frac{\varepsilon_{B\to J/\psi\to\mu\mu}}{\varepsilon_{\mathrm{prompt}J/\psi\to\mu\mu}}} \quad (9)$$

TABLE II. Parameters as defined in Eq. (3) and Eq. (4). Most of these parameters are fixed in preliminary steps. At the final fit stage, free parameters are $B \to J/\psi$ fraction ($F_{B\to J/\psi}$) (see text), the total J/ψ yields and $\sigma\prime$. Uncertainties are not only from the statistical fluctuations but also related with the systematic uncertainty evaluations.

Fit Parameter	$-2.2 < y < -1.2$	$1.2 < y < 2.2$
μ	-15 ± 5 μm	6 ± 5 μm
σ	209 ± 8 μm	210 ± 6 μm
μ_1	0 μm	0 μm
σ_1	60 ± 11 μm	50 ± 9 μm
$\sigma\prime$	7 ± 14 μm	10 ± 18 μm
μ_2	-135 ± 15 μm	-123 ± 18 μm
σ_2	169 ± 10 μm	150 ± 16 μm
α	0.74 ± 0.06	0.60 ± 0.08
n	3.50 ± 0.51	4.26 ± 0.75

H. Systematic uncertainty

The systematic uncertainty for $F_{B\to J/\psi}$ is evaluated by taking into account any factors which can affect the $\mathrm{DCA_R}$ mean, the $\mathrm{DCA_R}$ resolution, or the overall normalization of the signals. The following items are considered in the systematic uncertainty evaluation, along with a description of the methods performed to extract the uncertainties. For each item we compare the nominal $B \to J/\psi$ fraction extracted from our analysis to that obtained with alternate methods to extract the systematic uncertainty:

(a) p_T uncertainties: the B-meson $\to J/\psi$ p_T distributions were reweighted in $B \to J/\psi$ simulations according to the prompt J/ψ p_T distribution. The inclusive J/ψ p_T spectrum was also varied with different fractions of prompt J/ψ and B-meson $\to J/\psi$.

(b) Background determination uncertainties: smooth fit functions were used to characterize the combinatorial, mismatching and heavy flavor backgrounds instead of histograms and their effects on the fit result were evaluated.

(c) Background determination uncertainties: deviation of fit results from the average value with different fractions of $b\bar{b}$ contribution in the heavy flavor background. The $b\bar{b}$ fraction of the heavy flavor background was varied from 0, 50% to 100%. Even though the assumption of 0 or 100% $b\bar{b}$ heavy-flavor-continuum background is unrealistic, to be conservative, the maximum variation between the average value of the fitted B to J/ψ fraction and the fit result assuming 0 or 100% $b\bar{b}$ fraction of heavy flavor background is quoted as the systematic uncertainty.

(d) Background determination uncertainties: the combinatorial background normalization $\mathrm{Norm}_{\mathrm{mix}}$ defined in Eq. (2) was calculated within different dimuon mass ranges and compared to the nominal values.

(e) Fitting method uncertainties: multiple tests of the $\mathrm{DCA_R}$ fit function with varied $\mathrm{DCA_R}$ means and resolutions were applied to pseudodata, including different fractions of prompt J/ψ and J/ψ from B-meson decay with muon $\mathrm{DCA_R}$ shape determined in simulation and realistic backgrounds. The stability of the extracted ratios was checked and deviation from the average value is accounted for in the systematic uncertainty.

(f) Signal determination uncertainties: different functions were used to represent the muon $\mathrm{DCA_R}$ distributions in both prompt J/ψ and J/ψ from the B-meson decay events in simulation. A triple Gaussian function was used for prompt J/ψ events and a Crystal-Ball plus single Gaussian function was used for J/ψ from the B-meson decay events. The stability of the extracted ratios was checked.

(g) J/ψ selection uncertainties: good J/ψ candidates were selected in different dimuon pair mass windows (shifted by 0.15 GeV/c^2) and the extracted ratio results were compared to the nominal ratios.

(h) Alignment determination uncertainties: different misalignment residuals were applied to the $\mathrm{DCA_R}$ mean to determine their effect on the fit.

(i) Event quality cut uncertainties: different vertex resolution cuts were used and their effect on the fit evaluated.

(j) Dependence of simulation on different x-y vertex smearing: the vertex smearing was varied from the reconstructed value in real data (around 200 μm) to the average beam profile value (around 80 μm) and the effect on the fit evaluated.

(k) Variation of the acceptance × efficiency: the renormalization scale factors were varied in simulation to get different p_T distributions for prompt J/ψ and B-meson decays, then the acceptance × efficiency correction factors were recalculated and their effect on the fit was evaluated.

Table III gives the values and specific meanings for each evaluated contribution to the systematic uncertainty on the extracted fraction for J/ψ from B-meson decay. As indicated, the total systematic uncertainty is 1.9% in absolute scale for each muon arm in the $1.2 < |y| < 2.2$ rapidity coverage.

IV. RESULTS AND DISCUSSIONS

After applying the acceptance × efficiency factors shown in Table IV, the corrected $B \to J/\psi$ fraction in the rapidity interval $(1.2 < y < 2.2)$ is $7.8\% \pm 3.9\%(\mathrm{stat})$ and the fraction in the rapidity interval $(-2.2 < y < -1.2)$ is $8.3\% \pm 2.9\%(\mathrm{stat})$.

The final results are summarized in Table V. Because the $p + p$ system is symmetric, the results from the two arms are combined into a statistical average, giving a fraction of J/ψ from B-meson decays in the $1.2 < |y| < 2.2$ region of $8.1\% \pm 2.3\%(\mathrm{stat}) \pm 1.9\%(\mathrm{syst})$. This result is integrated in the interval $0 < p_T(J/\psi) < 5$ GeV/c.

TABLE III. Systematic uncertainty summary for the fraction of J/ψ from B-meson decay in the $1.2 < y < 2.2$ and $-2.2 < y < -1.2$ rapidity regions. Values are in absolute scale. See the specific meaning of each item in Sec. III H.

Source	$1.2 < y < 2.2$	$-2.2 < y < -1.2$	Specific Meaning
a	<0.1%	<0.1%	p_T uncertainties.
b	0.1%	0.2%	Background shape variations with fit functions.
c	1.4%	1.1%	$b\bar{b}$ fraction variations in the heavy flavor background.
d	<0.1%	<0.1%	Combinatorial background normalization variation.
e	0.5%	0.5%	Fit method variations.
f	0.3%	0.3%	Signal determination variations.
g	0.4%	0.5%	J/ψ selection variation.
h	0.3%	0.5%	Alignment correction variations.
i	0.4%	0.6%	Event quality cut variations.
j	1.0%	1.0%	Vertex smearing in the x-y plane.
k	0.1%	0.2%	Variations of the acceptance × efficiency.
Total systematic uncertainty	**1.9%**	**1.9%**	

TABLE IV. Relative ratio of acceptance × efficiency between prompt J/ψ and $B \to J/\psi$ events, uncorrected $B \to J/\psi$ fraction ($F^{\rm raw}_{B\to J/\psi}$) and corrected $B \to J/\psi$ fraction ($F_{B\to J/\psi}$). Uncertainties are statistical only.

	$\frac{A\varepsilon_{B\to J/\psi\to\mu\mu}}{A\varepsilon_{{\rm prompt}J/\psi\to\mu\mu}}$	$F^{\rm raw}_{B\to J/\psi}$	$F_{B\to J/\psi}$
$-2.2 < y < -1.2$	0.980 ± 0.022	$8.1\% \pm 2.8\%$	$8.3\% \pm 2.9\%$
$1.2 < y < 2.2$	0.935 ± 0.020	$7.3\% \pm 3.7\%$	$7.8\% \pm 3.9\%$

TABLE V. Fraction of B-meson decays in J/ψ samples obtained in $p+p$ collisions at $\sqrt{s} = 510$ GeV.

	$F_{B\to J/\psi}$
$-2.2 < y < -1.2$	$8.3\% \pm 2.9\%({\rm stat}) \pm 1.9\%({\rm syst})$
$1.2 < y < 2.2$	$7.8\% \pm 3.9\%({\rm stat}) \pm 1.9\%({\rm syst})$
$1.2 < \lvert y\rvert < 2.2$	$8.1\% \pm 2.3\%({\rm stat}) \pm 1.9\%({\rm syst})$

Comparisons to global measurements within the same inclusive J/ψ p_T region from CDF [3], ALICE [4], CMS [5] and LHCb [6,7] experiments are shown in Fig. 9(a). The result from PHENIX is also compared with the p_T-dependent fraction from other experiments using the average $p_T = 2.2$ GeV/c of our inclusive J/ψ sample as shown in Fig. 9(b). The LHCb experiment has measurements over a wide rapidity range, $2.0 < y < 4.5$; only results from $2.0 < y < 2.5$ and $3.0 < y < 3.5$ are shown in Fig. 9. The $2.0 < y < 2.5$ rapidity range is close to the kinematic range accessed by other measurements. The $F_{B\to J/\psi}$ result from this measurement is consistent with those from the higher energy collisions within uncertainties, although it does not exclude the possibility of a decrease of the $F_{B\to J/\psi}$ toward lower collision energy.

Figure 10 presents the comparison between the 510 GeV $p+p$ PHENIX result and the fixed-order-next-to-leading-log plus color-evaporation-model (FONLL + CEM) [12,21,22] predictions for the $B \to J/\psi$ fraction ($F_{B\to J/\psi}$) in 500 GeV $p+p$ collisions. The CEM J/ψ calculation uses the results of fitting the scale parameters to the energy dependence of the open charm total cross section for the charm quark mass $m_c = 1.27 \pm 0.09$ GeV/c^2. The factorization and renormalization scales, relative to the mass of the charm quark in the total cross section, were found to be $\mu_F/m = 2.1^{+2.55}_{-0.85}$ and $\mu_R/m = 1.6^{+0.11}_{-0.12}$ [22]. The same central values were used to fix the J/ψ normalization parameter in the CEM to the total cross section at $x_F > 0$ and $y > 0$ as a function of energy. The J/ψ distributions were calculated with the same mass and scale parameters but to include the p_T dependence instead of $\mu_{F,R}/m$, $\mu_{F,R}/m_T$ was used, where $m_T = \sqrt{(p^2_{T_c} + p^2_{T_{\bar{c}}})/2 + m_c^2}$. The shape of the p_T distribution at low p_T is determined by a k_T kick of 1.29 GeV/c at $\sqrt{s} = 500$ GeV. The energy difference between 500 and 510 GeV is small, so the difference in the $B \to J/\psi$ fraction is negligible. The measured fraction at PHENIX is consistent with the FONLL+CEM model prediction within uncertainties. The CMS nonprompt and prompt J/ψ cross section measurements at 7 TeV $p+p$ collisions [5] have been compared to the FONLL + CEM calculations as well. The old CEM

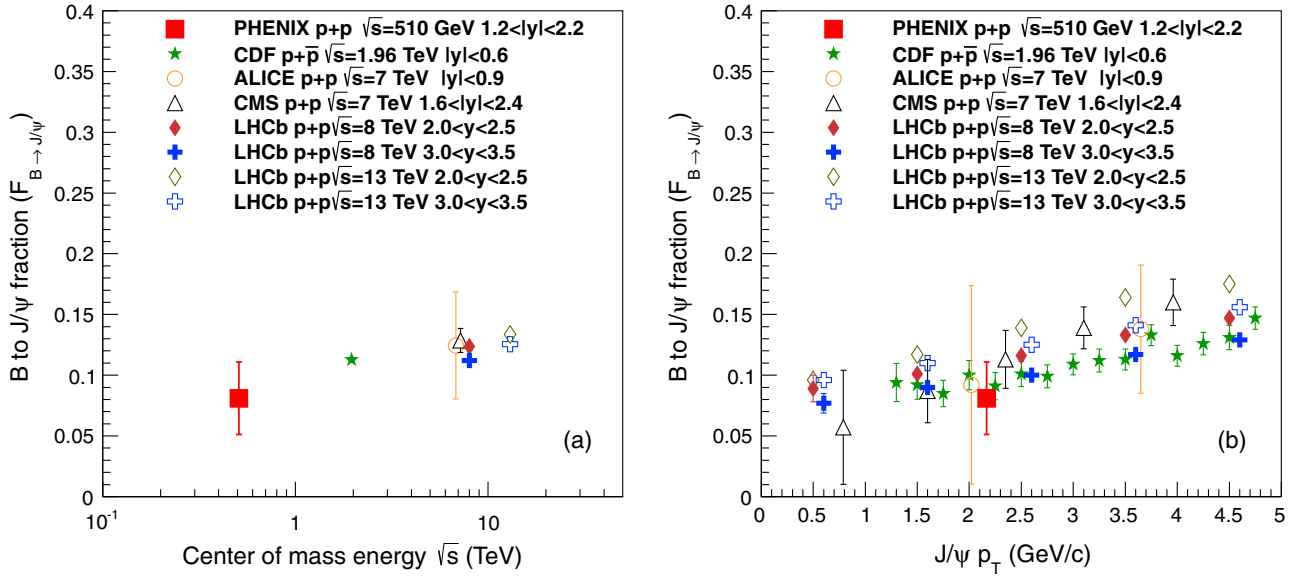

FIG. 9. Comparison of PHENIX $B \to J/\psi$ fraction with the global data from CDF [3], ALICE [4], CMS [5] and LHCb [6,7] experiments for J/ψ p_T and also with $0 < p_T < 5$ GeV/c, (a) as a function of center of mass energy integrated in the $J\psi$ interval $0 < p_T < 5$ GeV/c, and (b) as a function of inclusive J/ψ p_T. The uncertainty of the PHENIX measurement is statistical and systematic combined.

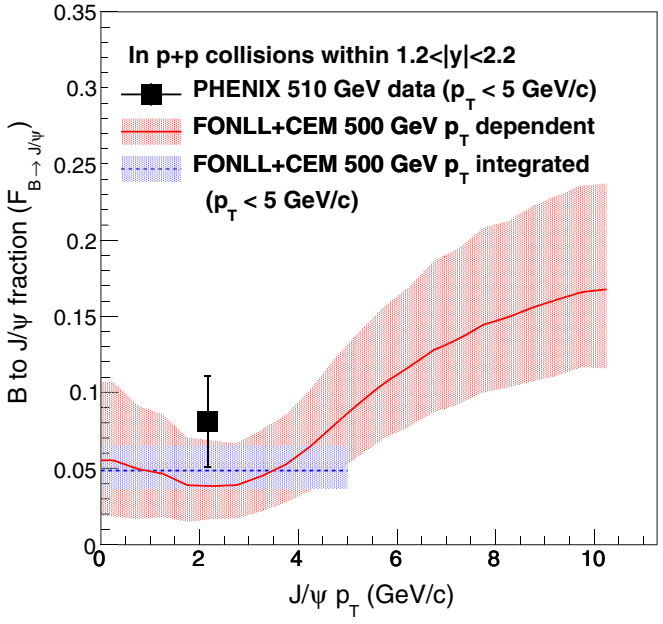

FIG. 10. In $p+p$ collisions at $\sqrt{s}=510$ GeV and $1.2<|y|<2.2$ rapidity region, comparison of PHENIX $B\to J/\psi$ fraction ($F_{B\to J/\psi}$) measured in integrated J/ψ p_T range of $p_T<5$ GeV/c with J/ψ p_T dependent (shown in solid red) and p_T integrated within 0–5 GeV/c region (shown in dashed blue) $B\to J/\psi$ fraction predicted by the FONLL + CEM [12,21,22] model in 500 GeV $p+p$ collisions. The uncertainty of the PHENIX measurement is statistical and systematic combined.

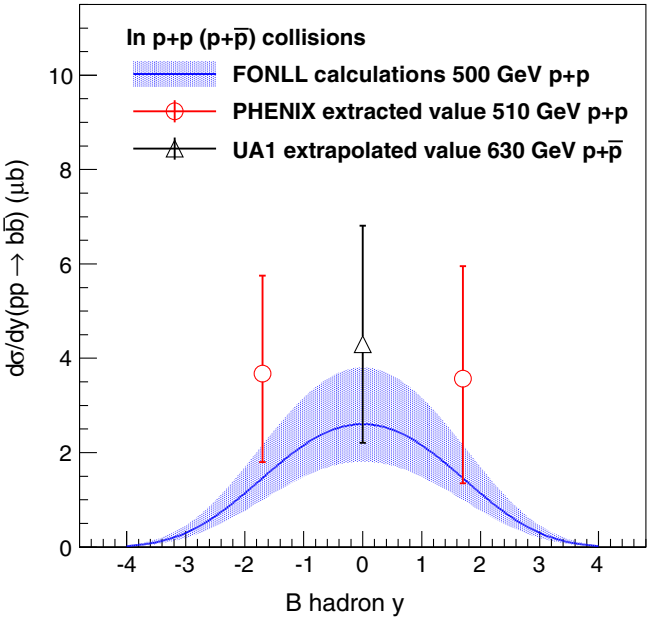

FIG. 11. The average $b\bar{b}$ cross section per unit rapidity [$d\sigma/dy(pp\to b\bar{b}+X)$] is determined by the $B\to J/\psi$ fraction ($F_{B\to J/\psi}$) discussed in the paper and the inclusive J/ψ cross section in 510 GeV $p+p$ collisions extrapolated from PHENIX 200 GeV $p+p$ measurements and the energy scaling factor provided by the CEM [22]. The extrapolated $d\sigma/dy(pp\to b\bar{b})$ (shown as open red circles) at B hadron mean rapidity $y=\pm1.7$ in 510 GeV $p+p$ collisions is compared with the rapidity-dependent B cross section (shown as blue solid line) calculated in FONLL. The PHENIX result is also comparable with the value of UA1 630 GeV $p+\bar{p}$ $d\sigma/dy(p\bar{p}\to b\bar{b})$ extracted from $p_T>8$ GeV/c to $p_T>0$ range [28,29] and unscaled with energy. The uncertainty of the extrapolated value at PHENIX (UA1) combines the statistical and systematic uncertainty from experiment with the CEM uncertainty. The uncertainty of the FONLL calculations contains both b quark mass and scaling uncertainties.

model underestimated the prompt J/ψ cross section within $1.6<|y|<2.4$ and J/ψ $p_T<5$ GeV/c region measured by the CMS experiment in 7 TeV $p+p$ collisions, while the nonprompt J/ψ cross section measured in the same kinematic region and experiment is consistent with the FONLL calculations. Calculations with the CEM parameters from [22] give a better agreement between the FONLL + CEM prediction and the $B\to J/\psi$ fraction measured by CMS [5]. The FONLL calculations can reasonably describe the nonprompt J/ψ cross section results at LHCb for $p_T>0$ [6,7].

The $B\to J/\psi$ fraction $F_{B\to J/\psi}$ is also related to the inclusive J/ψ cross section per unit rapidity $d\sigma/dy(pp\to J/\psi)$ and the $b\bar{b}$ cross section per unit rapidity $d\sigma/dy(pp\to b\bar{b})$,

$$F_{B\to J/\psi}=\frac{2\times d\sigma/dy(pp\to b\bar{b})\times \mathrm{Br}(B\to J/\psi+X)}{d\sigma/dy(pp\to J/\psi)}, \tag{10}$$

where $\mathrm{Br}(B\to J/\psi+X)$ is the branching ratio of B hadron decays to J/ψ and the b ($\bar{b}$) quark to B-hadron fragmentation is assumed to be 1. The factor of 2 in Eq. (10) accounts for the fact that both $B\to J/\psi$ and $\bar{B}\to J/\psi$ contribute to the $B\to J/\psi$ fraction $F_{B\to J/\psi}$. Equation (10) can be rewritten as

$$d\sigma/dy(pp\to b\bar{b})=\frac{\frac{1}{2}\times d\sigma/dy(pp\to J/\psi)\times F_{B\to J/\psi}}{\mathrm{Br}(B\to J/\psi+X)}. \tag{11}$$

Therefore, $d\sigma/dy(pp\to b\bar{b})$ can be derived from Eq. (11). To do this, we use $d\sigma/dy(pp\to J/\psi)=1.00\pm0.11$ μb (0.97 ± 0.11 μb) at mean rapidity $y=1.7$ (-1.7) in 510 GeV $p+p$ collisions, and $\mathrm{Br}(B\to J/\psi+X)=1.094\pm0.032\%$ [23]. Here, $d\sigma/dy(pp\to J/\psi,510\,\mathrm{GeV})$ is extrapolated as $d\sigma/dy(pp\to J/\psi,200\ \mathrm{GeV})\times R(510/200)$, where the scaling factor $R(510/200)$ is $2.08^{+0.75}_{-0.55}$ according to the CEM [22], and $d\sigma/dy(pp\to J/\psi,200\ \mathrm{GeV})=0.48\pm0.05$ μb (0.47 ± 0.05 μb) at mean rapidity $y=1.7$ (-1.7) [24].

The extracted $d\sigma/dy(pp\to b\bar{b})$ is $3.57^{+2.38}_{-2.22}(3.68^{+2.08}_{-1.88})$ μb at B hadron mean rapidity $=1.7$ (-1.7) in 510 GeV $p+p$ collisions. The weighted average of the two measurements is $d\sigma/dy(pp\to b\bar{b})=3.63^{+1.92}_{-1.70}$ μb at B-hadron rapidity $=\pm1.7$. As shown in Fig. 11, these values are comparable to

the FONLL-calculated rapidity-dependent B cross section within large uncertainties [25–27]. The PHENIX extracted values are also comparable to the UA1 $\sqrt{s} = 630$ GeV $p + \bar{p}$ average $b\bar{b}$ cross section per unit rapidity $[d\sigma/dy(p\bar{p} \to b\bar{b}, 630\ \text{GeV}) = 4.3^{+2.51}_{-2.10}\ \mu\text{b}]$ within $|y| < 1.5$ [28,29] which is extrapolated from $p_T > 8$ GeV/c to the $p_T > 0$ range. The FONLL calculation assumes $m_b = 4.75 \pm 0.25$ GeV/c^2 while the renormalization and factorization scales are varied by a factor of 2 around the central value, $\mu_{R,F} = \sqrt{p_T^2 + m_b^2}$ [12,27].

V. SUMMARY

We have presented a new measurement of the nonprompt over inclusive J/ψ production ratio $F_{B\to J/\psi}$ in $p + p$ collisions at $\sqrt{s} = 510$ GeV, integrated over the J/ψ kinematical domain, $p_T < 5$ GeV/c and rapidity $1.2 < |y| < 2.2$. The result is $F_{B\to J/\psi} = 8.1\% \pm 2.3\%(\text{stat}) \pm 1.9\%(\text{syst})$. This measurement extends the previously measured $F_{B\to J/\psi}$ values at CDF and LHC to lower energy, and is comparable to measurements at higher energies; it is also within 1.0 standard deviation of the FONLL + CEM calculation which has a non-negligible dependence on $\sqrt{s}$, p_T and y. The extrapolated $d\sigma/dy(pp \to b\bar{b})$ is $3.63^{+1.92}_{-1.70}\ \mu$b at B-hadron mean rapidity, ± 1.7, in 510 GeV $p + p$ collisions, which is comparable with the FONLL calculations in 500 GeV $p + p$ collisions.

The weak dependence on the center of mass energy in Fig. 9(a) for the $F_{B\to J/\psi}$ fraction could indicate that the variation of the bottom yield with energy is compensated by a similar variation of the prompt J/ψ yield. It is also noteworthy that only a factor of 2 decrease of the b over the c yield is expected going from LHC energies to $\sqrt{s} = 510$ GeV, as calculated with FONLL [25,26]. However, modeling the hadronization of the bound $c\bar{c}$ at low p_T is still a challenge to QCD calculations. The present results provide complementary information to the surprisingly weak evolution of $F_{B\to J/\psi}$ in $0.51 \le \sqrt{s} \le 13$ TeV domain, for central or near central rapidity and low p_T production.

The analysis procedure developed in this study will be applied to other data sets recorded by PHENIX at different center of mass energies. A similar method can also be applied to the study of B- and D-meson semileptonic decays to muons, which will help to understand the production mechanism of charm and bottom, and provide a complementary measurement to the one presented in this paper.

ACKNOWLEDGMENTS

We thank the staff of the Collider-Accelerator and Physics Departments at Brookhaven National Laboratory and the staff of the other PHENIX participating institutions for their vital contributions. We acknowledge support from the Office of Nuclear Physics in the Office of Science of the Department of Energy, the National Science Foundation, Abilene Christian University Research Council, Research Foundation of SUNY, and Dean of the College of Arts and Sciences, Vanderbilt University (U.S.A), Ministry of Education, Culture, Sports, Science, and Technology and the Japan Society for the Promotion of Science (Japan), Conselho Nacional de Desenvolvimento Científico e Tecnológico and Fundação de Amparo à Pesquisa do Estado de São Paulo (Brazil), Natural Science Foundation of China (People's Republic of China), Croatian Science Foundation and Ministry of Science and Education (Croatia), Ministry of Education, Youth and Sports (Czech Republic), Centre National de la Recherche Scientifique, Commissariat à l'Énergie Atomique, and Institut National de Physique Nucléaire et de Physique des Particules (France), Bundesministerium für Bildung und Forschung, Deutscher Akademischer Austausch Dienst, and Alexander von Humboldt Stiftung (Germany), National Science Fund, OTKA, EFOP, and the Ch. Simonyi Fund (Hungary), Department of Atomic Energy and Department of Science and Technology (India), Israel Science Foundation (Israel), Basic Science Research Program through NRF of the Ministry of Education (Korea), Physics Department, Lahore University of Management Sciences (Pakistan), Ministry of Education and Science, Russian Academy of Sciences, Federal Agency of Atomic Energy (Russia), VR and Wallenberg Foundation (Sweden), the U.S. Civilian Research and Development Foundation for the Independent States of the Former Soviet Union, the Hungarian American Enterprise Scholarship Fund, and the US-Israel Binational Science Foundation.

[1] F. Abe *et al.* (CDF Collaboration), Measurement of Bottom Quark Production in 1.8 TeV $p\bar{p}$ Collisions Using Semileptonic Decay Muons, Phys. Rev. Lett. **71**, 2396 (1993).

[2] S. Abachi *et al.* (D0 Collaboration), J/ψ production in $p\bar{p}$ collisions at $\sqrt{s} = 1.8$-TeV, Phys. Lett. B **370**, 239 (1996).

[3] D. Acosta *et al.* (CDF Collaboration), Measurement of the J/ψ meson and b-hadron production cross sections in $p\bar{p}$

collisions at $\sqrt{s} = 1960$ GeV, Phys. Rev. D **71**, 032001 (2005).

[4] B. Abelev *et al.* (ALICE Collaboration), Measurement of prompt J/ψ and beauty hadron production cross sections at mid-rapidity in pp collisions at $\sqrt{s} = 7$ TeV, J. High Energy Phys. 11 (2012) 065.

[5] V. Khachatryan *et al.* (CMS Collaboration), Prompt and non-prompt J/ψ production in pp collisions at $\sqrt{s} = 7$ TeV, Eur. Phys. J. C **71**, 1575 (2011).

[6] R. Aaij *et al.* (LHCb Collaboration), Production of J/ψ and Upsilon mesons in pp collisions at $\sqrt{s} = 8$ TeV, J. High Energy Phys. 06 (2013) 064.

[7] R. Aaij *et al.* (LHCb Collaboration), Measurement of forward J/ψ production cross-sections in pp collisions at $\sqrt{s} = 13$ TeV, J. High Energy Phys. 10 (2015) 172.

[8] G. Aad *et al.* (ATLAS Collaboration), Measurement of the differential cross-sections of prompt and non-prompt production of J/ψ and $\psi(2S)$ in pp collisions at $\sqrt{s} = 7$ and 8 TeV with the ATLAS detector, Eur. Phys. J. C **76**, 283 (2016).

[9] C. Albajar *et al.* (UA1 Collaboration), J/ψ and ψ' production at the CERN p anti-p collider, Phys. Lett. B **256**, 112 (1991).

[10] E. Norrbin and T. Sjostrand, Production and hadronization of heavy quarks, Eur. Phys. J. C **17**, 137 (2000).

[11] L. Adamczyk *et al.* (STAR Collaboration), J/ψ production at high transverse momenta in $p + p$ and Au + Au collisions at $\sqrt{s_{NN}} = 200$ GeV, Phys. Lett. B **722**, 55 (2013).

[12] M. Cacciari, P. Nason, and R. Vogt, QCD Predictions for Charm and Bottom Quark Production at RHIC, Phys. Rev. Lett. **95**, 122001 (2005).

[13] M. Allen *et al.*, PHENIX inner detectors, Nucl. Instrum. Methods Phys. Res., Sect. A **499**, 549 (2003).

[14] H. Akikawa *et al.*, PHENIX Muon Arms, Nucl. Instrum. Methods Phys. Res., Sect. A **499**, 537 (2003).

[15] M. Baker *et al.* (PHENIX Collaboration), BNL Internal Report No. 72204.

[16] A. Adare *et al.* (PHENIX Collaboration), Single electron yields from semileptonic charm and bottom hadron decays in Au + Au collisions at $\sqrt{s_{NN}} = 200$ gev, Phys. Rev. C **93**, 034904 (2016).

[17] C. Aidala *et al.*, The PHENIX Forward Silicon Vertex Detector, Nucl. Instrum. Methods Phys. Res., Sect. A **755**, 44 (2014).

[18] T. Sjostrand, S. Mrenna, and P. Z. Skands, A brief introduction to PYTHIA 8.1, Comput. Phys. Commun. **178**, 852 (2008).

[19] S. Agostinelli *et al.*, GEANT4: A simulation toolkit, Nucl. Instrum. Methods Phys. Res., Sect. A **506**, 250 (2003).

[20] K. A. Dress and S. White, Vernier scan results from the first rhic proton run at 250 gev, in IPAC10 Proceedings, 2010 (unpublished).

[21] M. Bedjidian *et al.*, Hard probes in heavy ion collisions at the LHC: Heavy flavor physics, arXiv:hep-ph/0311048.

[22] R. E. Nelson, R. Vogt, and A. D. Frawley, Narrowing the uncertainty on the total charm cross section and its effect on the J/ψ cross section, Phys. Rev. C **87**, 014908 (2013).

[23] C. Patrignani *et al.* (Particle Data Group), The review of particle physics, Chin. Phys. C **40**, 100001 (2016).

[24] A. Adare *et al.* (PHENIX Collaboration), Ground and excited charmonium state production in $p + p$ collisions at $\sqrt{s} = 200$ GeV, Phys. Rev. D **85**, 092004 (2012).

[25] M. Cacciari, M. Greco, and P. Nason, The p_T spectrum in heavy-flavour hadroproduction, J. High Energy Phys. 05 (1998) 007.

[26] M. Cacciari, S. Frixione, and P. Nason, The p_T spectrum in heavy flavor photoproduction, J. High Energy Phys. 03 (2001) 006.

[27] M. Cacciari, S. Frixione, N. Houdeau, M. L. Mangano, P. Nason, and G. Ridolfi, Theoretical predictions for charm and bottom production at the LHC, J. High Energy Phys. 10 (2012) 137.

[28] C. Albajar *et al.* (UA1 Collaboration), Beauty production at the CERN pp collider, Phys. Lett. B **256**, 121 (1991).

[29] C. Albajar *et al.* (UA1 Collaboration), Measurement of $b\bar{b}$ correlations at the CERN $p\bar{p}$ collider, Z. Phys. C **61**, 41 (1994).